

# JGR Atmospheres

## RESEARCH ARTICLE

10.1029/2019JD031736

### Key Points:

- In addition to GHGs, CA wintertime precipitation increases under sulfate forcing, particularly European and Asian sulfate
- In contrast, black carbon aerosols decrease California precipitation
- California precipitation is more sensitive to aerosols than to GHGs and solar forcing

### Supporting Information:

- Supporting Information S1

### Correspondence to:

R. J. Allen,  
rjallen@ucr.edu

### Citation:

Allen, R. J., Lamarque, J.-F., Watson-Parris, D., & Olivie, D. (2020). Assessing California wintertime precipitation responses to various climate drivers. *Journal of Geophysical Research: Atmospheres*, 125, e2019JD031736. <https://doi.org/10.1029/2019JD031736>

Received 25 SEP 2019

Accepted 13 MAY 2020

Accepted article online 21 MAY 2020

## Assessing California Wintertime Precipitation Responses to Various Climate Drivers

Robert J. Allen<sup>1</sup> , Jean-Francois Lamarque<sup>2</sup> , Duncan Watson-Parris<sup>3</sup> , and Dirk Olivie<sup>4</sup>

<sup>1</sup>Department of Earth and Planetary Sciences, University of California Riverside, Riverside, CA, USA, <sup>2</sup>NCAR/UCAR, Boulder, CO, USA, <sup>3</sup>Atmospheric, Oceanic & Planetary Physics, Department of Physics, University of Oxford, Oxford, UK, <sup>4</sup>Norwegian Meteorological Institute, Oslo, Norway

**Abstract** Understanding how drivers of climate change affect precipitation remains an important area of research. Although several robust precipitation responses have been identified under continued increases in greenhouse gases (GHGs), considerable uncertainty remains. This is particularly the case at regional scales, including the West Coast of the United States and California. Here, we exploit idealized, single forcing simulations from the Precipitation Driver Response Model Intercomparison Project (PDRMIP) to address how climate drivers impact California wintertime precipitation. Consistent with recent work, GHGs including carbon dioxide and methane, as well as solar forcing, yield a robust increase in California wintertime precipitation. We also find robust California precipitation responses to aerosols but with opposite responses for sulfate versus black carbon aerosol. Sulfate aerosol increases California wintertime precipitation, whereas black carbon reduces it. Moreover, California precipitation is more sensitive to aerosols, particularly regional emissions from Europe and Asia, than to GHGs. These precipitation responses are consistent with shifts in the jet stream and altered moisture fluxes. Although the idealized nature of PDRMIP simulations precludes a formal attribution, our results suggest that aerosols can perturb precipitation and fresh water resources along the West Coast of the United States.

## 1. Introduction

Understanding how climate change impacts the hydrological cycle, including precipitation patterns and fresh water resources, remains an important societal issue. Model simulations and theoretical considerations show robust precipitation perturbations in a warmer world, including drying of the subtropics and wetting of the middle to high latitudes (Collins et al., 2013; Meehl et al., 2007). This enhancement of the pattern of precipitation minus evaporation (i.e., wet regions get wetter and dry regions drier) is largely a consequence of the increase in horizontal moisture transport under warming, due to the increase in lower-tropospheric water vapor (Held & Soden, 2006).

Although robust precipitation responses also exist at regional scales, including drying of the Mediterranean and the southwest United States (Cayan et al., 2010; Cook et al., 2015; Hoerling et al., 2012; Polade et al., 2017; Seager et al., 2010), regional precipitation responses remain relatively uncertain. This includes the West Coast of the United States, and in particular California—the fifth largest economy in the world and a major agricultural center. Although observations indicate negligible long-term changes over the entire 20th century, substantial multidecadal California precipitation variability exists (Bedsworth et al., 2018). Twenty-first century model projections, particularly those from the Coupled Model Intercomparison Project version 5 (CMIP5) (Taylor et al., 2012), indicate an increase in California wintertime precipitation in response to continued greenhouse gas (GHG) emissions (Allen & Luptowitz, 2017; Neelin et al., 2013), including an increase in extreme precipitation (Polade et al., 2017; Zecca et al., 2018) associated with atmospheric rivers (Dettinger, 2011; Hagos et al., 2016; Lavers et al., 2015). However, other seasons, particularly spring, are likely to become drier (Gao et al., 2014), indicating an intensification of the wet-dry seasonal cycle (Allen & Anderson, 2018), more dry spells and floods (Swain et al., 2018), and an increase in summertime California drought (Diffenbaugh et al., 2015).

In addition to GHGs, atmospheric aerosols are also capable of perturbing the hydrological cycle and have likely masked the expected increase in global mean precipitation due to GHGs (Liepert et al., 2004; Richardson et al., 2018; Salzmann, 2016; Wu et al., 2013). Moreover, shortwave climate drivers, like aerosols,

have a larger apparent hydrological sensitivity (defined as the change in precipitation per unit change in global surface temperature) than longwave drivers, such as GHGs (Andrews et al., 2010; Liepert & Previdi, 2009; Liu et al., 2018; Samset et al., 2016). Hemispheric contrasts in aerosols have also shifted the tropical rain band, contributing to the Sahel drought that peaked in the mid-1980s (Allen et al., 2015; Ackerley et al., 2011; Biasutti & Giannini, 2006; Chang et al., 2011; Frierson & Hwang, 2012; Hwang et al., 2013; Undorf et al., 2018). Several studies also show the role of aerosols in reducing monsoon precipitation. The observed precipitation reduction in recent decades over the South and East Asia monsoon regions can be explained by the dominance of aerosol radiative effects suppressing precipitation over the expected enhancement due to increasing GHGs (Krishnan et al., 2016; Li et al., 2015; Lau & Kim, 2017; Lin et al., 2018).

The Precipitation Driver Response Model Intercomparison Project (PDRMIP) (Myhre et al., 2017) consists of a suite of idealized, single-forcing model simulations to understand how various climate drivers impact global and regional precipitation. In addition to the aforementioned studies, recent PDRMIP analyses have also shown aerosols can perturb regional precipitation patterns, including weakening of the Asian monsoon in response to sulfate aerosol (Liu et al., 2018; Samset et al., 2016). PDRMIP simulations also suggest that the increase in black carbon aerosols have contributed to Mediterranean drying (Tang et al., 2018). This signal was related to a positive North Atlantic Oscillation pattern, associated with a poleward shift of the jet stream and storm track.

Here, we leverage the PDRMIP archive to quantify how various climate drivers, including GHGs as well as aerosols, impact U.S. West Coast precipitation, focused on California. The paper is organized as follows: Section 2 describes the PDRMIP models and simulations used in this study. Results are presented in section 3, focused on the California wintertime precipitation response to various climate drivers, as well as the associated dynamical changes including atmospheric winds and moisture flux. A discussion and conclusion follow in sections 4 and 5, respectively.

## 2. Methods and Data

### 2.1. Model Simulations

The PDRMIP models and experimental design is described by Myhre et al. (2017). In summary, up to ten climate models (Table 1) performed several idealized, single-forcing simulations, including a control simulation with all anthropogenic and natural forcing agents set to present day values, a doubling of carbon dioxide ( $2\times\text{CO}_2$ ), a tripling of methane ( $3\times\text{CH}_4$ ), and a 2% increase in total solar irradiance (Solar+2%). Aerosol experiments include a fivefold increase in anthropogenic sulfate concentrations or emissions ( $5\times\text{SO}_4$ ) and a 10-fold increase in anthropogenic black carbon concentrations or emissions ( $10\times\text{BC}$ ). Most of the PDRMIP models (seven of the 10) also performed regional aerosol experiments, including a 10-fold increase in European sulfate concentrations/emissions ( $10\times\text{SO}_4$  Europe), a 10-fold increase in Asian sulfate concentrations/emissions ( $10\times\text{SO}_4$  Asia), and a 10-fold increase in Asian black carbon concentrations/emissions ( $10\times\text{BC}$  Asia). The European (Asian) region is defined from 35–70N and 10W to 40E (10–50N and 60–140E).

In terms of the aerosol simulations, some models are driven by changes in aerosol concentrations, whereas others are driven by changes in aerosol emissions. Concentration-driven models use identical AeroCom-based fixed concentrations in the control simulation; the anthropogenic part of these concentrations is multiplied by a factor (e.g., 10 in  $10\times\text{BC}$  experiment) to obtain the perturbation simulation. Emission-driven models use individual emissions for the control simulation; these emissions are multiplied by a factor to obtain the perturbation. Most models' control simulation is based on present-day aerosols; an exception is HadGEM2-ES, which uses year 1860 emissions for the control simulation but year 2000 emissions for the experiment (Stjern et al., 2017). In the emission-driven models, the climate response to the increase in aerosols (e.g., BC-induced warming and altered precipitation) can feedback on the aerosol concentrations (e.g., via modified aerosol wet removal), dampening or amplifying the climate response (Allen et al., 2016, 2019; Sand et al., 2015). No model includes aerosol indirect effects on convective precipitation. GISS-E2-R is the lone model that lacks aerosol indirect effects. All models use a dynamic ocean model, except CESM-CAM4 and ECHAM-HAM, both of which use a slab ocean.

### 2.2. Methods

Both coupled ocean-atmosphere and fixed sea surface temperature (SST) simulations were performed. The former give the total climate response (experiment minus control), whereas the latter give the fast response

**Table 1**  
**PDRMIP Models Used in This Study**

Model	Version	Resolution	Aerosol mode/size bin	Mixing state	Regional simulations	References
CanESM (E)	2010	2.8 × 2.8; 35 levels	S, N, BC, OC, DU, SS	Internal	No	Arora et al. (2011)
HadGEM2 (E)	6.6.3	1.875 × 1.25; 38 levels	S(G), BC, OC, BB(3), DU(6), SS(2)	External	No	Collins et al. (2011)
MIROC-SPRINTARS (E)	5.9.0	~1.4 × 1.4; 40 levels	S(1), BC(1), OC(1), DU(6) SS(4)	Internal and external	Yes	Takemura et al. (2005, 2009)
CESM-CAM5 (E)	1.1.2	2.5 × 1.9; 30 levels	S, BC, POM, SOA, SS, DU(3)	Internal	Yes	Hurrell et al. (2013)
ECHAM-HAM(E)	6.3/2.2	~1.8 × 1.8; 31 & 47 levels	S(4), BC(4), POM(4), SOA(20), DU(4), SS(2)	Internal and external	No	Zhang et al. (2012)
CESM-CAM4 (C)	1.0.3	2.5 × 1.9; 26 levels	S, BC(2), POM(2), SOA, DU(4), SS(4)	External	Yes	Neale et al. (2010)
GISS-E2R (C)	E2-R	2 × 2.5; 40 levels	S(1), N(1), BC(1), OC(1), DU(4), SS(2)	Internal and external	Yes	Schmidt et al. (2014)
HadGEM3 (C)	GA 4.0	1.875 × 1.25; 85 levels	S(G), BC, OC, BB(3), DU(6), SS(2)	External	Yes	Bellouin et al. (2011)
NorESM (C)	1-M	2.5 × 1.9; 26 levels	S, BC, OM, SS, DU 13 modes, 33 size bins	Internal and external	Yes	Bentsen et al. (2013)
IPSL-CM5A (C)	CMIP5	3.75 × 1.875; 39 levels	S, BC, OC, DU, SS	External	Yes	Dufresne et al. (2013)

*Note.* Emission (concentration) driven models are indicated with an “E” (“C”). All models used a coupled ocean, except CESM-CAM4 and ECHAM-HAM, which implemented a slab ocean. All models use a log-normal aerosol size distribution. Microphysical aerosol interactions with clouds (aerosol indirect effects) are accounted for in all models except GISS-E2R. In addition to lacking regional aerosol simulations, ECHAM-HAM also lacks 5sSO<sub>4</sub> and Solar+2% simulations. Abbreviations: BB, biomass burning; BC, black carbon; DU, dust; GA, global atmosphere; N, nitrate; OC, organic carbon; OM, organic mass; POM, primary organic matter; S, sulfate; SOA, secondary organic aerosol; SS, sea salt.

(rapid adjustments). Coupled simulations were run for 100 years, and we analyze the last 50 years. Fixed SST simulations are integrated for 15 years. Except for the effective radiative forcing (ERF) calculation, which is derived from the fixed SST simulations, all analyses are based on the coupled model simulations. Statistical significance of the ensemble mean response is based on a  $t$  test for the difference of means (experiment minus control) using the pooled variance. We also quantify the robustness of the response by the percentage of models that agree on the sign of the change. We define a “robust” response as one in which at least 70% of models agree on the sign of the response. Our definition of “robust” is consistent with Intergovernmental Panel on Climate Change’s (IPCC) definition of “likely,” where 2/3 model agreement is required (Cubasch et al., 2013). Our definition of robust, however, is less stringent than IPCC’s definition of “very likely,” where 9/10 model agreement is required. All model data are spatially interpolated to a  $2.5 \times 2.5^\circ$  grid using bilinear interpolation. To maximize the use of available data, ensemble means are constructed by averaging over all available models. This implies that a slightly different mix of models constitutes the ensemble mean, depending on the experiment (e.g., only seven of the 10 PDRMIP models performed regional aerosol simulations).

### 3. Results

#### 3.1. ERF

Figure S1 in the supporting information shows the ensemble mean annual mean ERF map for each experiment (see also Myhre et al., 2017). The ERF for each model and experiment is also included in Tables S1 and S2. ERF has been shown to be more representative of the eventual temperature response to climate drivers and is estimated from the top-of-the-atmosphere (TOA) radiative perturbation (change in net radiative longwave plus shortwave fluxes) from the corresponding fixed SST simulations (Forster et al., 2016). The multimodel mean ERF (and the range) is  $3.72$  ( $3.32$  to  $4.32$ )  $\text{W m}^{-2}$  for  $2\times\text{CO}_2$ ;  $1.21$  ( $0.86$  to  $1.49$ )  $\text{W m}^{-2}$  for  $3\times\text{CH}_4$ ; and  $4.17$  ( $4.01$  to  $4.40$ ) for Solar+2%. The global aerosol simulations yield corresponding ERFs of  $-3.51$  ( $-8.27$  to  $-2.04$ )  $\text{W m}^{-2}$  for  $5\times\text{SO}_4$  and  $1.01$  ( $0.39$  to  $1.54$ )  $\text{W m}^{-2}$  for  $10\times\text{BC}$ . The regional aerosol simulations yield corresponding ERFs of  $0.15$  ( $0.004$  to  $0.40$ )  $\text{W m}^{-2}$  for  $10\times\text{BC}$  Asia;  $-0.74$  ( $-1.15$  to  $-0.45$ )  $\text{W m}^{-2}$  for  $10\times\text{SO}_4$  Asia; and  $-0.35$  ( $-0.47$  to  $-0.25$ )  $\text{W m}^{-2}$  for  $10\times\text{SO}_4$  Europe. We note larger model disagreement among global annual mean ERF for the aerosol simulations relative to the GHG/solar experiments.

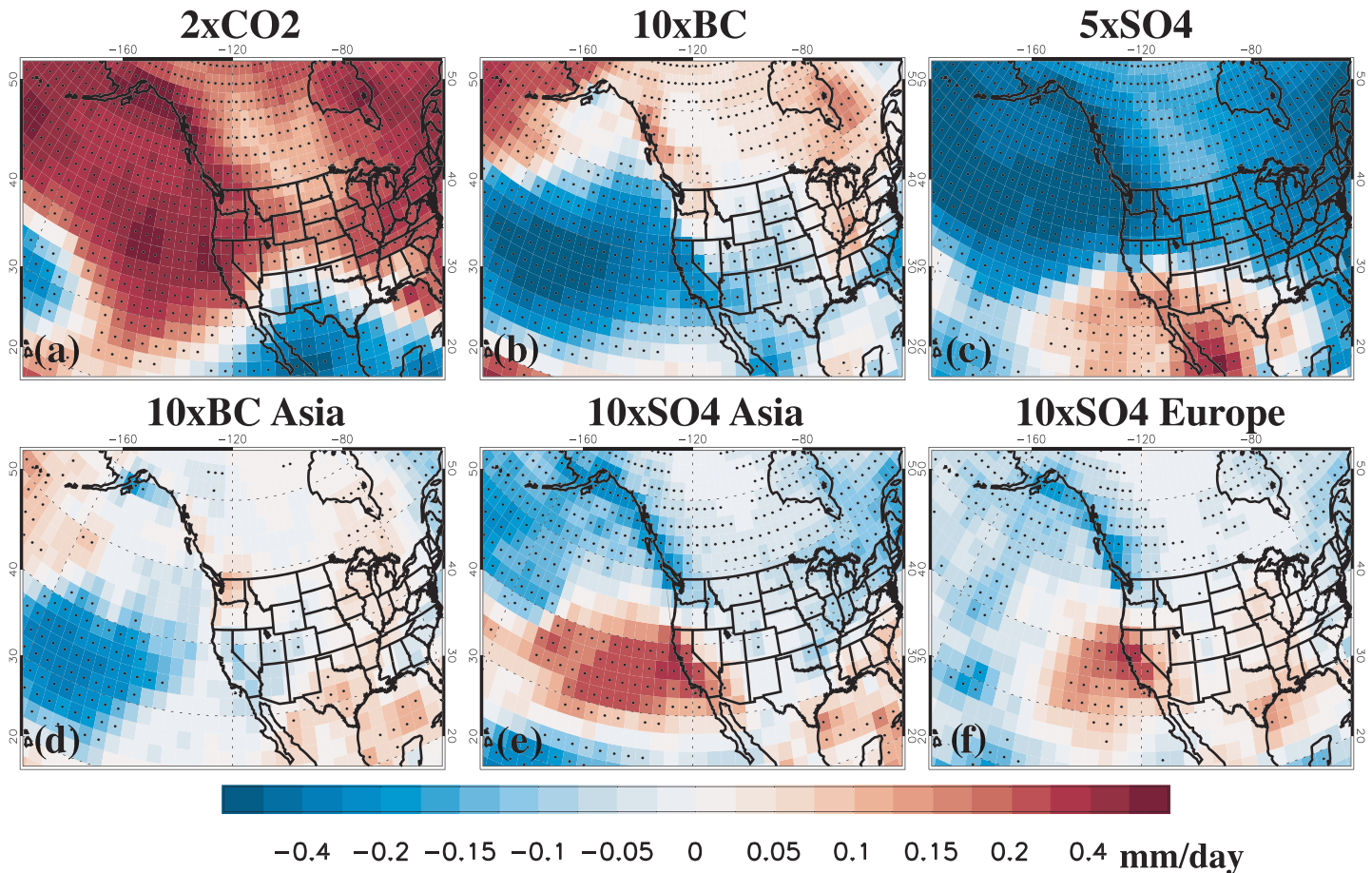
#### 3.2. Precipitation Response

Figure 1 shows the wintertime (November through March, NDJFM) ensemble mean precipitation response for several climate drivers.  $2\times\text{CO}_2$  yields a significant increase in precipitation for most of the North American West Coast, including California, with drying in Mexico and parts of the southern United States. Wintertime wetting of California in response to future increases in GHGs, as well as more idealized increases in GHGs (i.e., 1% per year  $\text{CO}_2$  increases), is consistent with prior studies based on models from the CMIP5 (Allen & Luptowitz, 2017; Allen & Anderson, 2018; Neelin et al., 2013; Zecca et al., 2018). In addition to  $2\times\text{CO}_2$ , PDRMIP models also show increases in wintertime California precipitation for both  $3\times\text{CH}_4$  and Solar+2% (Figure S2).

Less is known about the possible impact of aerosols on West Coast precipitation. PDRMIP simulations show that aerosols drive significant California wintertime precipitation responses, with  $10\times\text{BC}$  leading to drying for most of the U.S. West Coast, particularly California, as well as drying of the southwestern United States and Mexico. In contrast,  $5\times\text{SO}_4$  leads to a West Coast dipole pattern of wetting (drying) south (north) of  $\sim 40^\circ\text{N}$ . Mexico and Baja California experience the largest increase in precipitation. Similar precipitation responses are generally obtained when models are subdivided into concentration- versus emission-driven models (Figure S3). There are some differences, however, including a larger increase in California precipitation in response to  $5\times\text{SO}_4$  in the emission-driven models. In contrast, concentration-driven models yield a larger (and more robust) decrease in California precipitation in response to  $10\times\text{BC}$ . Some of this precipitation response contrast is due to model differences independent of the experimental design (e.g., MIROC-SPRINTARS  $10\times\text{BC}$  yields relatively large California wetting, to be discussed below).

In addition to the global aerosol simulations, PDRMIP also conducted several regional aerosol simulations, focusing on the main centers of historical aerosol emissions, Europe and Asia (unfortunately, no U.S. regional experiments were performed).  $10\times\text{BC}$  Asia drives relatively weak California drying that extends



Ensemble Mean NDJFM  $\Delta$ Precipitation

**Figure 1.** Wintertime ensemble mean precipitation response to (a)  $2\times\text{CO}_2$ ; (b)  $10\times\text{BC}$ ; (c)  $5\times\text{SO}_4$ ; (d)  $10\times\text{BC}$  Asia; (e)  $10\times\text{SO}_4$  Asia; and (f)  $10\times\text{SO}_4$  Europe. Wintertime is defined as November through March. Changes significant at the 90% confidence level are denoted by black dots, based on a  $t$  test for the difference of means using the pooled variance. Units are  $\text{mm day}^{-1}$ .

to the Four Corners region, but most of the drying is located over the Pacific Ocean. Both  $10\times\text{SO}_4$  Asia and Europe lead to significant wetting that is centered on California. Figure 2 shows the corresponding wintertime precipitation response model agreement. Except in the case of  $10\times\text{BC}$  Asia, at least 70% of the models support the aforementioned California precipitation signals, indicating a “robust” PDRMIP response. Thus, PDRMIP simulations suggest aerosols can perturb West Coast precipitation, including California.

Recall that a subset of PDRMIP models performed the regional aerosol simulations (Table 1; seven of the 10). Thus, the ensemble mean plots in Figure 1 are based on slightly different models, particularly the global versus regional aerosol ensemble mean plots. Figure S4 shows that the ensemble mean change in wintertime precipitation for  $2\times\text{CO}_2$ ,  $10\times\text{BC}$ , and  $5\times\text{SO}_4$  is similar using all models or when restricted to the seven models with regional aerosol simulations. Furthermore, the differing California precipitation response to  $10\times\text{BC}$  versus  $10\times\text{BC}$  Asia is not due to the different mix of models. Similar California drying is obtained under  $10\times\text{BC}$  when the ensemble mean is restricted to the same seven models used to construct the  $10\times\text{BC}$  Asia ensemble mean. The reason for this difference is that unlike most models, MIROC-SPRINTARS simulates relatively large West Coast wetting in response to BC, particularly  $10\times\text{BC}$  Asia. Reasons for this model's different behavior are unclear, but this model also simulates the opposite east Pacific circulation responses to BC (next sections). Removing MIROC-SPRINTARS from the ensemble mean results in significant California drying under  $10\times\text{BC}$  Asia (Figure S4).

Although there is a robust California precipitation response to most of the climate drivers ( $10\times\text{BC}$  Asia being the exception), Figure 3 shows that for nearly all of the climate drivers, there are models that yield a

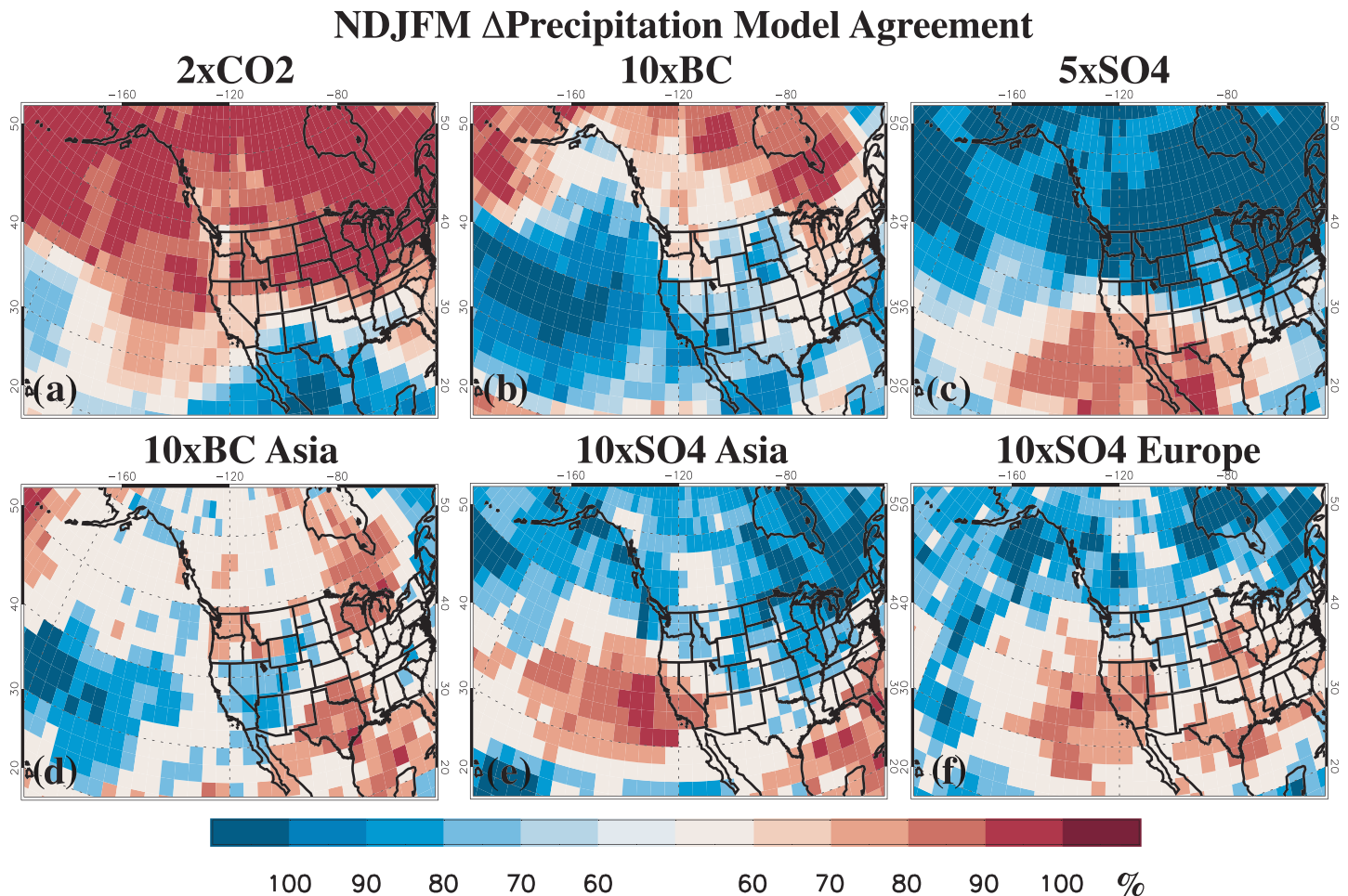


**Figure 2.** Wintertime precipitation response model agreement for (a)  $2\times\text{CO}_2$ ; (b)  $10\times\text{BC}$ ; (c)  $5\times\text{SO}_4$ ; (d)  $10\times\text{BC}$  Asia; (e)  $10\times\text{SO}_4$  Asia; and (f)  $10\times\text{SO}_4$  Europe. Wintertime is defined as November through March. Warm (cold) colors show the percent of models that yield an increase (decrease) in precipitation.

California precipitation response that is opposite to the majority of the models. This includes the GHG simulations, as well as Solar+2%, where NorESM1, ECHAM-HAM, and GISS-E2-R yield drying or negligible change. The ensemble mean California precipitation response to  $5\times\text{SO}_4$  is near zero, consistent with the dipole pattern of wetting (drying) south (north) of  $\sim 40^\circ\text{N}$ . HadGEM3, however, yields a very large drying trend. Although we do not find significant intermodel correlations between a model's ERF and its California precipitation response for a given experiment (not shown), we note that HadGEM3 is also an outlier in terms of the  $5\times\text{SO}_4$  ERF. At  $-8.27\text{ Wm}^{-2}$ , it is nearly double the multimodel mean  $5\times\text{SO}_4$  ERF. For the BC simulations, the aforementioned MIROC-SPRINTARS model stands out as driving wetting, especially for  $10\times\text{BC}$  Asia, in contrast to most of the models. More consistency across models exists in the regional sulfate simulations. Figure 3 also shows similar results exist for the 95th percentile of daily wintertime precipitation. Climate drivers that yield an increase (decrease) in NDJFM California mean precipitation also yield a corresponding increase (decrease) in extreme precipitation.

We also quantify the California precipitation response for the traditionally defined boreal fall (September–October–November, SON) and spring (March–April–May, MAM) seasons (Figure S5). For MAM,  $2\times\text{CO}_2$ ,  $3\times\text{CH}_4$ , and Solar+2% yield ensemble mean California drying (in contrast to the NDJFM wetting). Although these ensemble mean responses are not significant, 80% (78%) of the models yield drying for  $2\times\text{CO}_2$  (Solar+2%). The  $\text{CO}_2$  response is consistent with prior studies noting a “robust spring drying” of the southwestern United States, which was attributed to strengthening and expansion of the subtropical high pressure in the Pacific and Atlantic (Gao et al., 2014).  $10\times\text{BC}$  and  $10\times\text{BC}$  Asia also yield ensemble mean MAM drying, with 100% and 85% model agreement, respectively. The sulfate experiments yield ensemble mean MAM wetting, with robust responses for  $5\times\text{SO}_4$  and  $10\times\text{SO}_4$  Asia (88% and 85% model agreement, respectively).

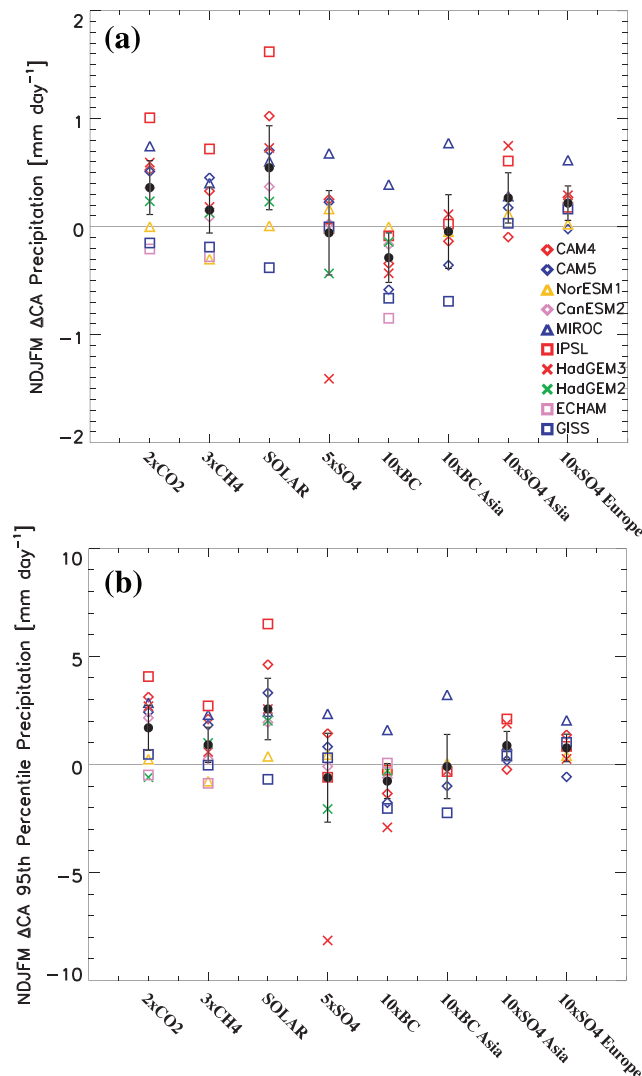


**Figure 3.** Wintertime California (a) mean and (b) 95th percentile precipitation response for the eight climate drivers. Each model is represented by a symbol, as indicated in the legend. The corresponding ensemble mean response is shown as a black circle, including the approximate 90% confidence interval, estimated as  $2\sigma/\sqrt{n}$ , where  $\sigma$  is the intermodel standard deviation and  $n$  is the number of models. California is defined as 33.75N and 241.25–243.75E; 36.25N and 238.75–241.25E; and 38.75–41.25N and 236.25–238.75E. Wintertime is defined as November through March. Units are  $\text{mm day}^{-1}$ .

Similar but less robust results exist for SON. This includes ensemble mean SON drying for  $2x\text{CO}_2$ ,  $3x\text{CH}_4$ , and Solar+2%, as well as for  $10x\text{BC}$  and  $10x\text{BC Asia}$ . Ensemble mean SON wetting occurs for  $5x\text{SO}_4$ ,  $10x\text{SO}_4$  Asia, and  $10x\text{SO}_4$  Europe. Thus, BC ( $\text{SO}_4$ ) experiments yield California drying (wetting) throughout the entire California wet season, including fall, winter, and spring. GHGs and solar forcing yield wetting during winter but drying during spring and fall.

Figure 4 (see also Figures S6 and S7) shows the NDJFM California large-scale and convective precipitation responses. Except for  $5x\text{SO}_4$ , similar signed ensemble mean NDJFM California precipitation responses occur for both large-scale and convective precipitation. For  $\text{CO}_2$ , the bulk (81%) of the ensemble mean total precipitation increase is due to an increase in convective precipitation. For  $\text{CH}_4$  and Solar+2%, the ensemble mean increase in both convective and large-scale precipitation is similar, but the convective precipitation increase is more robust (80% model agreement for both  $\text{CH}_4$  and Solar+2%) than the large-scale precipitation increase (60% and 56%, respectively).

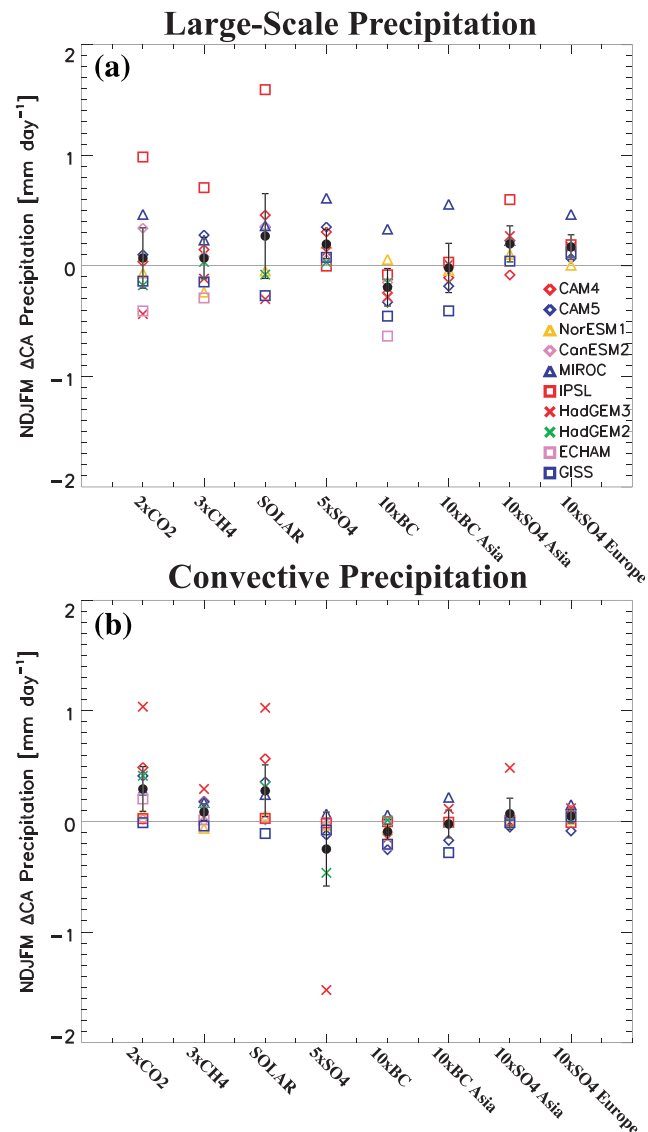


**Figure 4.** Wintertime California (a) large-scale and (b) convective precipitation response for the eight climate drivers. Each model is represented by a symbol, as indicated in the legend. The corresponding ensemble mean response is shown as a black circle, including the approximate 90% confidence interval, estimated as  $2\sigma/\sqrt{n}$ , where  $\sigma$  is the intermodel standard deviation and  $n$  is the number of models. California is defined as 33.75N and 241.25–243.75E; 36.25N and 238.75–241.25E; and 38.75–41.25N and 236.25–238.75E. Wintertime is defined as November through March. Units are  $\text{mm day}^{-1}$ .

For the aerosol experiments, however, the ensemble mean California NDJFM large-scale precipitation response tends to be larger and more robust than the corresponding convective precipitation response. For 10xBC (10xBC Asia), the ensemble mean decrease in large-scale precipitation is 66% (52%) of the total decrease. Model agreement is the same for both convective and large-scale precipitation at 80% for 10xBC and 71% for 10xBC Asia. For 10xSO<sub>4</sub> Asia and Europe, the ensemble mean increase in large-scale precipitation is 74% of the total increase, with larger model agreement for large-scale, as opposed to convective precipitation. 5xSO<sub>4</sub> is the lone experiment that yields opposite signed California NDJFM ensemble mean large-scale and convective precipitation responses. These responses are similar in magnitude and model agreement (e.g., 89% model agreement for the large-scale precipitation increase and the convective precipitation decrease). Similar conclusions exist between emissions- versus concentration-driven 5xSO<sub>4</sub> models.



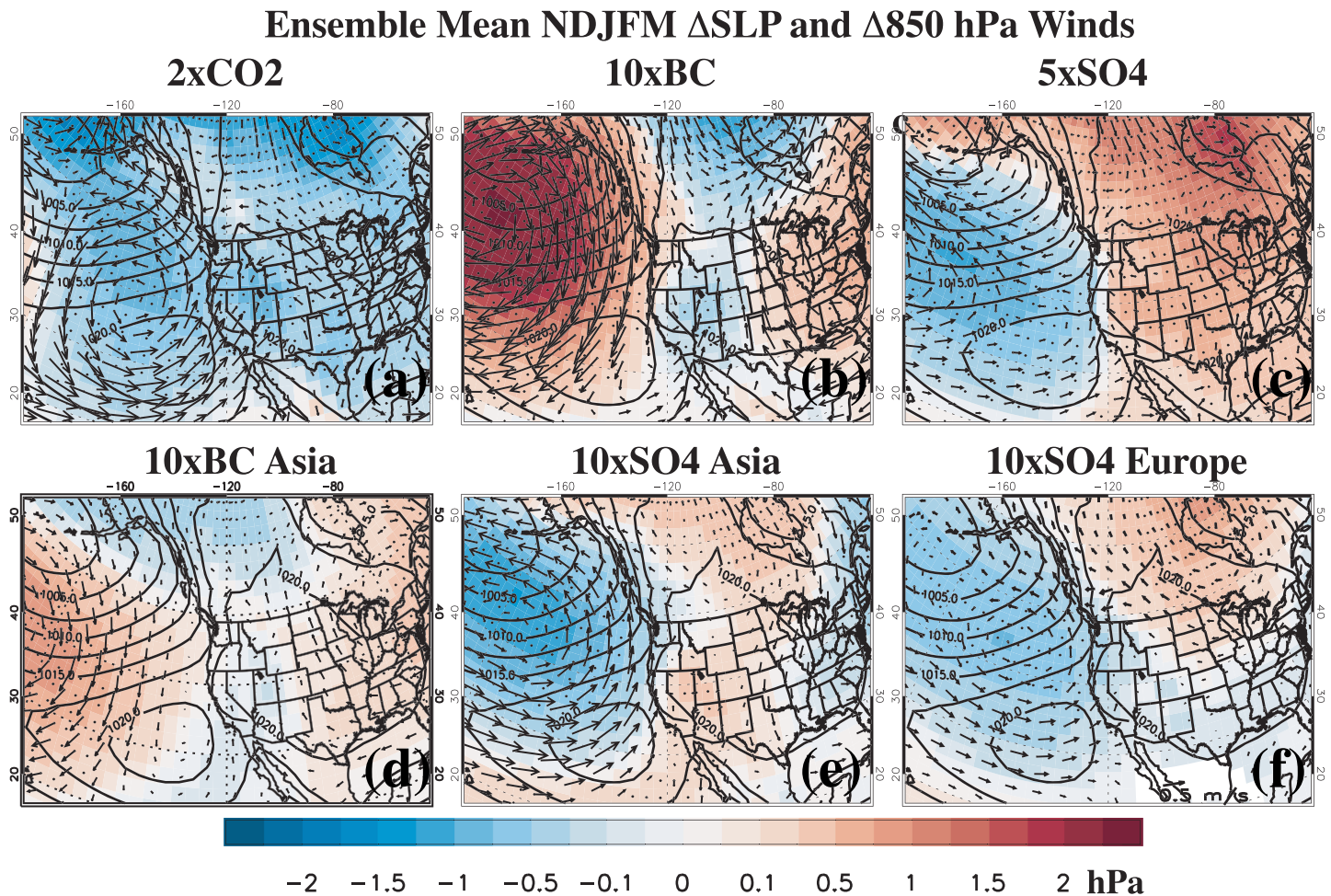


**Figure 5.** Wintertime ensemble mean sea level pressure (SLP) and 850-hPa wind response to (a) 2xCO<sub>2</sub>; (b) 10xBC; (c) 5xSO<sub>4</sub>; (d) 10xBC Asia; (e) 10xSO<sub>4</sub> Asia; and (f) 10xSO<sub>4</sub> Europe. Wintertime is defined as November through March. Black contours indicate the climatological wintertime ensemble mean SLP. Black arrows indicate 850-hPa wind response. SLP changes significant at the 90% confidence level are denoted by black dots, based on a *t* test for the difference of means using the pooled variance. SLP units are hectopascals; wind units are m s<sup>-1</sup>.

To summarize, California NDJFM wetting is mostly due to an increase in convective precipitation under GHG and solar forcing, particularly for CO<sub>2</sub>. In contrast, the California wintertime precipitation response under aerosol forcing is mostly due to changes in large-scale precipitation. 5xSO<sub>4</sub> yields opposite signed changes for convective and large-scale precipitation, with the change in large-scale (convective) precipitation driving the increase (decrease) in total precipitation for southern (northern) California (Figure 1).

### 3.3. Sea Level Pressure and Wind Response

Figure 5 shows the wintertime ensemble mean sea level pressure (SLP) and 850-hPa wind response (Figure S8 shows the corresponding SLP response model agreement). The climate drivers that enhance California wintertime precipitation, including CO<sub>2</sub> and sulfate, feature a deepening and southeastward shift of the Aleutian low. In turn, the 850-hPa winds show enhanced counterclockwise circulation, with anomalous southwesterly winds off the California coast. Similar responses exist for both CH<sub>4</sub> and Solar+2% (Figure S9). In contrast, the drivers that reduce California wintertime precipitation, particularly BCx10, yield a weakening of the Aleutian low and anomalous clockwise flow, including northerly/northeasterly flow near the California coast. These changes are barotropic in nature, as they also exist in the tropospheric geopotential height response (not shown).

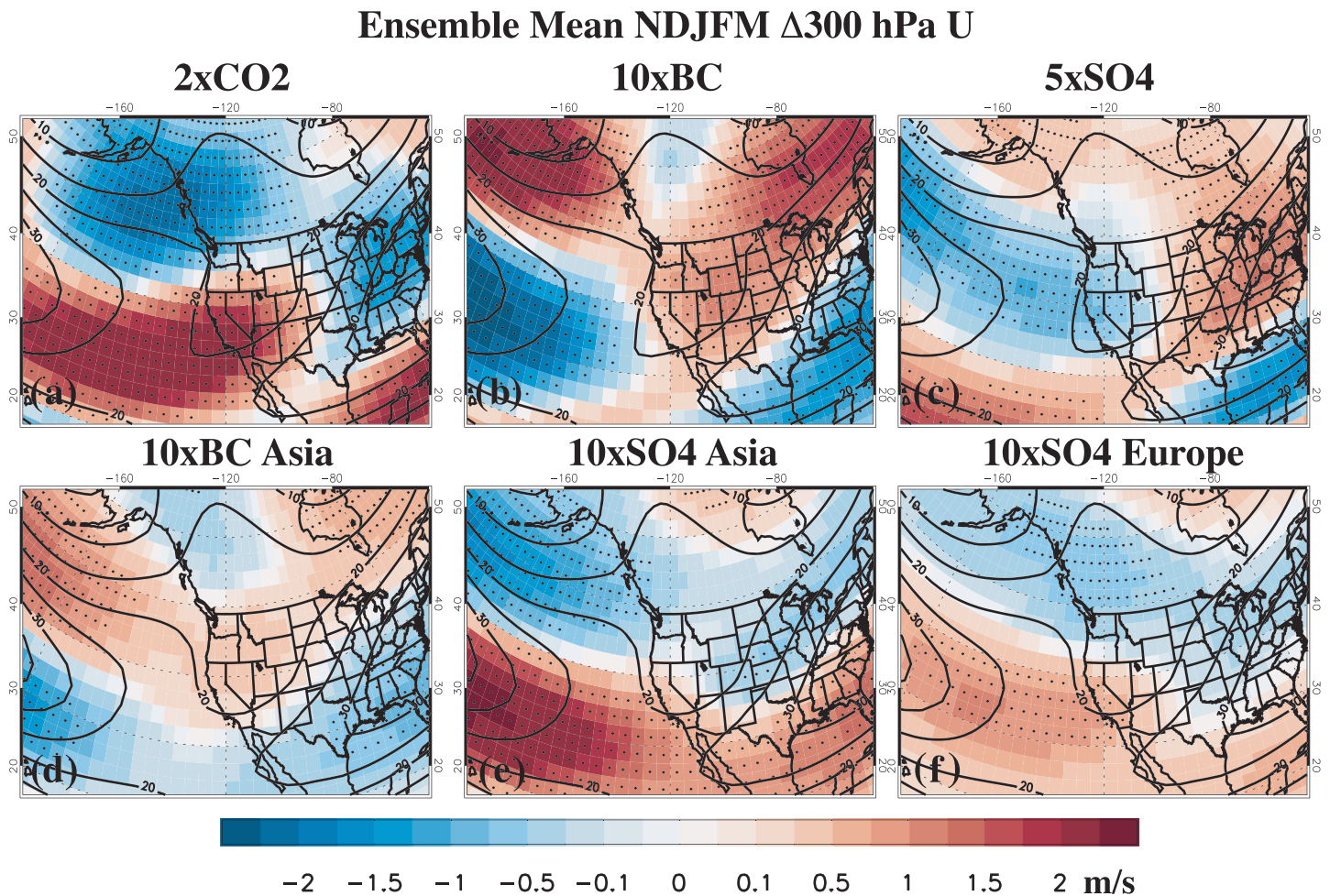


**Figure 6.** Wintertime ensemble mean 300-hPa zonal wind ( $U$ ) response to (a)  $2\times\text{CO}_2$ ; (b)  $10\times\text{BC}$ ; (c)  $5\times\text{SO}_4$ ; (d)  $10\times\text{BC}$  Asia; (e)  $10\times\text{SO}_4$  Asia; and (f)  $10\times\text{SO}_4$  Europe. Wintertime is defined as November through March. Black contours indicate the climatological wintertime ensemble mean 300-hPa  $U$ . Changes significant at the 90% confidence level are denoted by black dots, based on a  $t$  test for the difference of means using the pooled variance. Units are  $\text{m s}^{-1}$ .

In addition to these near-surface atmospheric dynamical changes, the 300-hPa zonal winds—which are important for controlling the location of the storm track and steering midlatitude cyclones—also show robust responses. Figure 6 shows that  $\text{CO}_2$  drives a southward shift/southeastward extension of the jet stream (Figure S10 shows the model agreement). This response is consistent with prior studies and was suggested to promote the increase in California precipitation under continued GHG-induced warming (Chang et al., 2015; Neelin et al., 2013). PDRMIP simulations also show that similar results exist for both  $\text{CH}_4$  and Solar+2% (Figure S11). For the aerosol simulations,  $5\times\text{SO}_4$  drives a southward shift of the jet, with decreases in 300-hPa zonal winds on the poleward flank of the climatological jet and increases on the equatorward jet flank. Sulfate regional simulations, including  $5\times\text{SO}_4$  Asia and Europe, also yield an equatorward jet displacement, in addition to an eastward extension of the jet. The southward shift of the Pacific jet in  $5\times\text{SO}_4$  is larger than in the regional sulfate simulations and possibly related to U.S. sulfate emissions. In contrast to sulfate aerosol,  $10\times\text{BC}$  again leads to the opposite response, including a poleward shift of the jet stream.  $10\times\text{BC}$  Asia also leads to a poleward jet shift, but it is primarily confined to the east Pacific.

### 3.4. Moisture Flux Response

At monthly time scales ( $>10$  days), the atmospheric moisture budget indicates that precipitation, evaporation, and net moisture flux into/out of an atmospheric column are in a balance (Trenberth & Guillemot, 1995). The atmospheric moisture balance is written as  $Pr = -\nabla \cdot MF + E$ , where  $Pr$  is precipitation,  $E$  is



## Ensemble Mean NDJFM $\Delta$ MFC

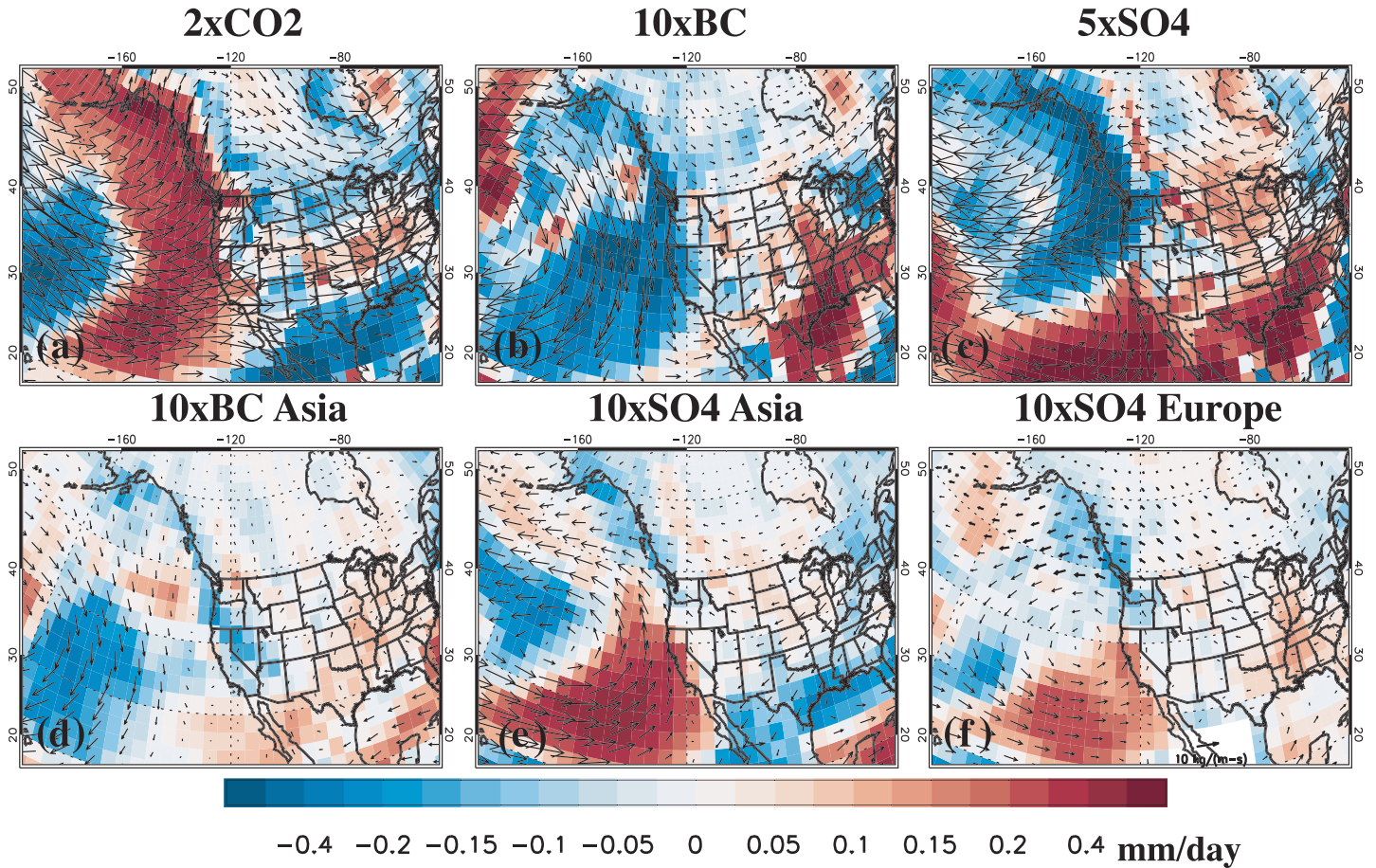


**Figure 7.** Wintertime ensemble mean moisture flux convergence (MFC) response to (a)  $2\times\text{CO}_2$ ; (b)  $10\times\text{BC}$ ; (c)  $5\times\text{SO}_4$ ; (d)  $10\times\text{BC}$  Asia; (e)  $10\times\text{SO}_4$  Asia; and (f)  $10\times\text{SO}_4$  Europe. Wintertime is defined as November through March. Arrows show the moisture flux response. MFC units are  $\text{mm day}^{-1}$ .

surface evaporation, and  $-\nabla \cdot \mathbf{MF}$  is the vertically integrated moisture flux convergence (MFC). The vertically integrated moisture flux MF is defined as

$$\mathbf{MF} = \int_{p_t}^{p_s} \frac{Q\mathbf{V}}{g} dp, \quad (1)$$

where  $p_s$  is surface pressure (1,000 hPa),  $p_t$  is 100 hPa,  $p$  is pressure,  $dp$  is the difference in pressure between layers,  $g$  is the gravitational acceleration ( $9.81 \text{ ms}^{-2}$ ),  $Q$  is specific humidity ( $\text{kg kg}^{-1}$ ), and  $\mathbf{V}$  is the horizontal wind vector ( $\text{m s}^{-1}$ ). Pressure levels used to calculate MF include 1,000, 925, 850, 700, 600, 500, 400, 300, 250, 200, and 100 hPa. Ideally, MF and MFC are estimated from submonthly data due to the nonlinear  $Q\mathbf{V}$  term. However, PDRMIP models only archived monthly mean wind and humidity fields, so our moisture flux calculations represent the mean component only (no transient component). Furthermore, two models lacked specific humidity data, so it was calculated from temperature, relative humidity, and pressure. MFC is calculated from the divergence of MF (multiplied by -1), using centered finite differences.

Figure 7 shows the moisture flux and the corresponding MFC.  $2\times\text{CO}_2$  leads to enhanced westerly/southwesterly moisture flux along the West Coast, as well as MFC (as does  $3\times\text{CH}_4$  and Solar+2%, Figure S12).  $5\times\text{SO}_4$  also shows an increase in southwesterly moisture flux and convergence for most of California and Baja California, with the opposite response poleward of  $\sim 40^\circ\text{N}$ .  $10\times\text{SO}_4$  Asia and Europe lead to a similar increase in southwesterly moisture flux and convergence for California.  $10\times\text{BC}$  leads to the opposite response, and relatively weak changes exist for  $10\times\text{BC}$  Asia (except off the coast). These responses are consistent with the patterns of precipitation change and to the dynamical changes (SLP and winds) previously described.

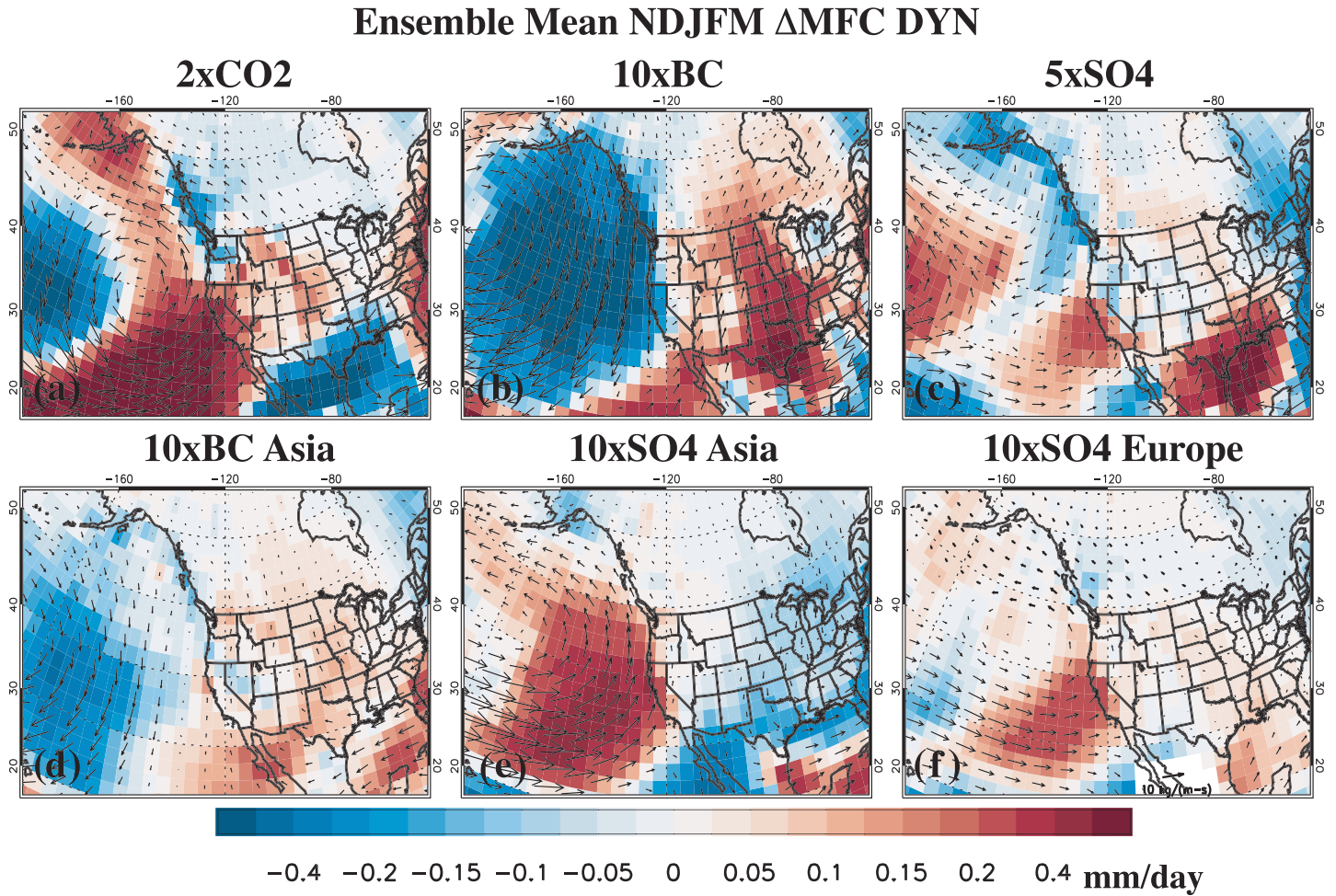


**Figure 8.** Wintertime ensemble mean dynamic component of moisture flux convergence (MFC DYN) response to (a)  $2\times\text{CO}_2$ ; (b)  $10\times\text{BC}$ ; (c)  $5\times\text{SO}_4$ ; (d)  $10\times\text{BC}$  Asia; (e)  $10\times\text{SO}_4$  Asia; and (f)  $10\times\text{SO}_4$  Europe. Wintertime is defined as November through March. Arrows show the dynamic component of the moisture flux response. MFC units are  $\text{mm day}^{-1}$ .

The mean MF is determined by both specific humidity and wind velocity. These two variables are associated with thermodynamic and dynamic aspects of the atmosphere, respectively. To investigate the relative roles of thermodynamic versus dynamic processes on the mean MF (Payne & Magnusdottir, 2015; Seager et al., 2010, 2014), we approximate the change in MF as

$$\delta MF \approx \frac{1}{g} \int_{p_t}^{p_s} [\delta Q \bar{V} + \bar{Q} \delta V] dp, \quad (2)$$

where  $\delta(\bullet)$  is the difference between experiment and control simulations (e.g.,  $\delta(\bullet) = (\bullet)_{10\times\text{BC}} - (\bullet)_{\text{control}}$ ) and the overbars represent the climatological wintertime average from the control simulation. The first term of equation (2) represents the thermodynamic response; the second term represents the dynamic response. The corresponding thermodynamic and dynamic MFCs are estimated by taking the divergence of the above equation and multiplying by -1.

Figure 8 shows the dynamical contribution to the change in moisture flux and its convergence (Figure S13 shows the thermodynamic contribution). Consistent with the large circulation changes off the California coast in response to the various climate drivers, most of the total moisture flux response and its convergence is due to dynamics, as opposed to thermodynamics. Similar conclusions exist for  $\text{CH}_4$  and Solar+2% (Figure S12). This highlights the importance of dynamical changes (i.e., changes in the SLP and winds) in driving the California precipitation responses. For  $5\times\text{SO}_4$ , the increase in MF and MFC in southern California (where precipitation increases) is largely consistent with the dynamical component; however, the



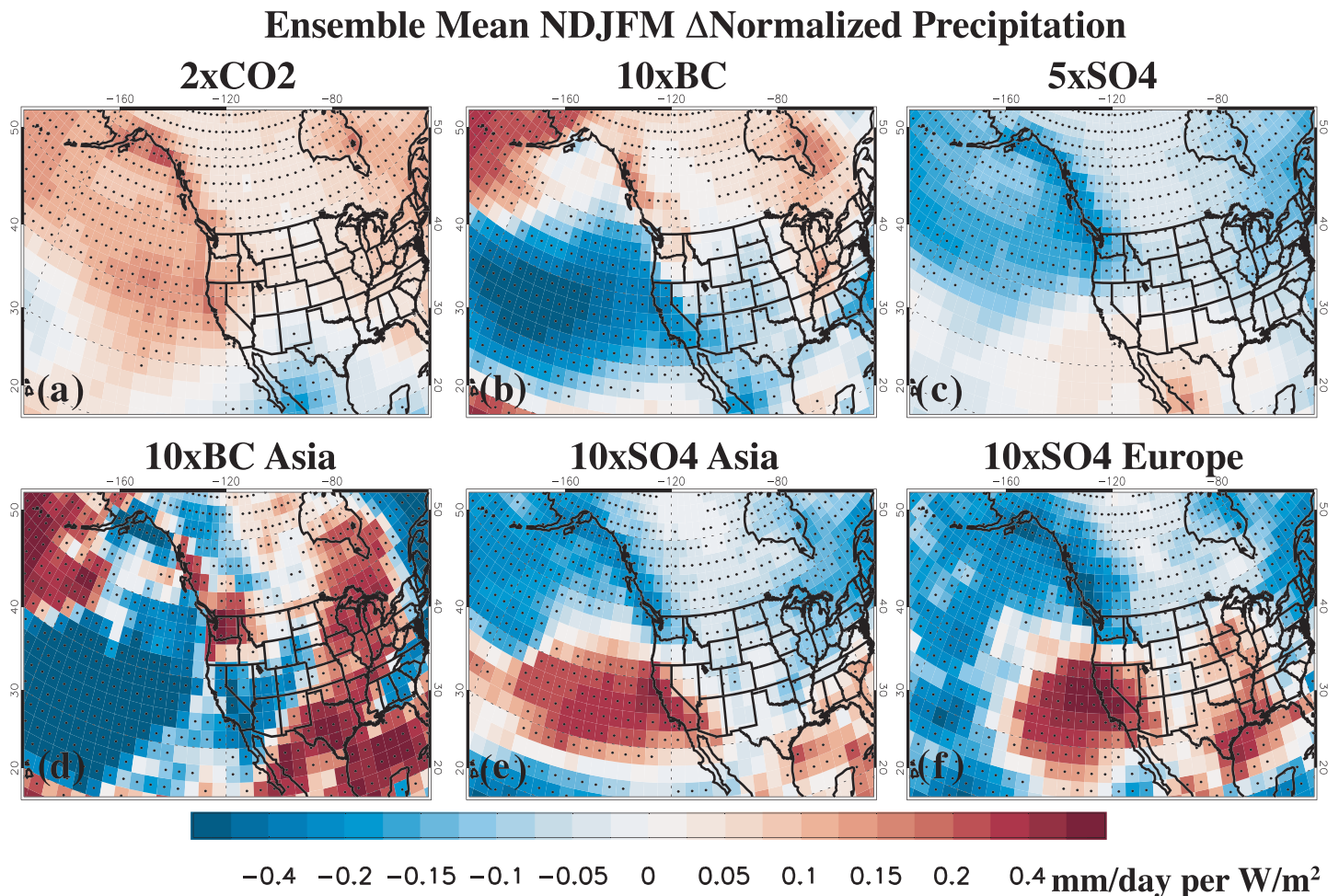


**Figure 9.** Wintertime ensemble mean normalized precipitation response to (a)  $2\times\text{CO}_2$ ; (b)  $10\times\text{BC}$ ; (c)  $5\times\text{SO}_4$ ; (d)  $10\times\text{BC}$  Asia; (e)  $10\times\text{SO}_4$  Asia; and (f)  $10\times\text{SO}_4$  Europe. Precipitation responses have been normalized by the ensemble mean annual mean effective radiative forcing (ERF). Wintertime is defined as November through March. Changes significant at the 90% confidence level are denoted by black dots, based on a  $t$  test for the difference of means using the pooled variance. Units are  $\text{mm day}^{-1}$  per  $\text{W m}^{-2}$ .

decrease in MF and MFC in northern California (where precipitation decreases) is largely consistent with the thermodynamic component.

### 3.5. Normalized Precipitation Response

Figure 9 shows the ensemble mean NDJFM normalized precipitation responses to the various climate drivers. Here, the change in precipitation is normalized by the ensemble mean annual mean ERF (section 3.1). Relative to  $\text{CO}_2$ , as well as  $3\times\text{CH}_4$  and Solar+2% (not shown), aerosols drive a larger California precipitation response per unit ERF. In particular, California precipitation is most sensitive to regional aerosols but with opposite responses between BC and sulfate. The much larger increase in California normalized precipitation in  $10\times\text{SO}_4$  Asia and  $10\times\text{SO}_4$  Europe, relative to  $5\times\text{SO}_4$ , illustrates how the relatively small sulfate forcing in Asia and Europe (relative to the global sulfate forcing) is very efficient at perturbing West Coast precipitation. This further suggests the possible importance of aerosols, particularly those emitted from Europe and Asia, in perturbing California precipitation. The relatively large response in most of the regional aerosol simulations also highlights the importance of the location of the aerosol forcing. This is consistent with prior work showing midlatitude aerosol forcing is capable of meridionally shifting the latitude of the maximum meridional temperature gradient and, in turn, the latitude of the jet stream which steers precipitation-bearing extratropical storms (Allen et al., 2012a, 2012b; Allen & Ajoku, 2016; Kovilakam & Mahajan, 2015). This will be discussed in more detail in section 4.

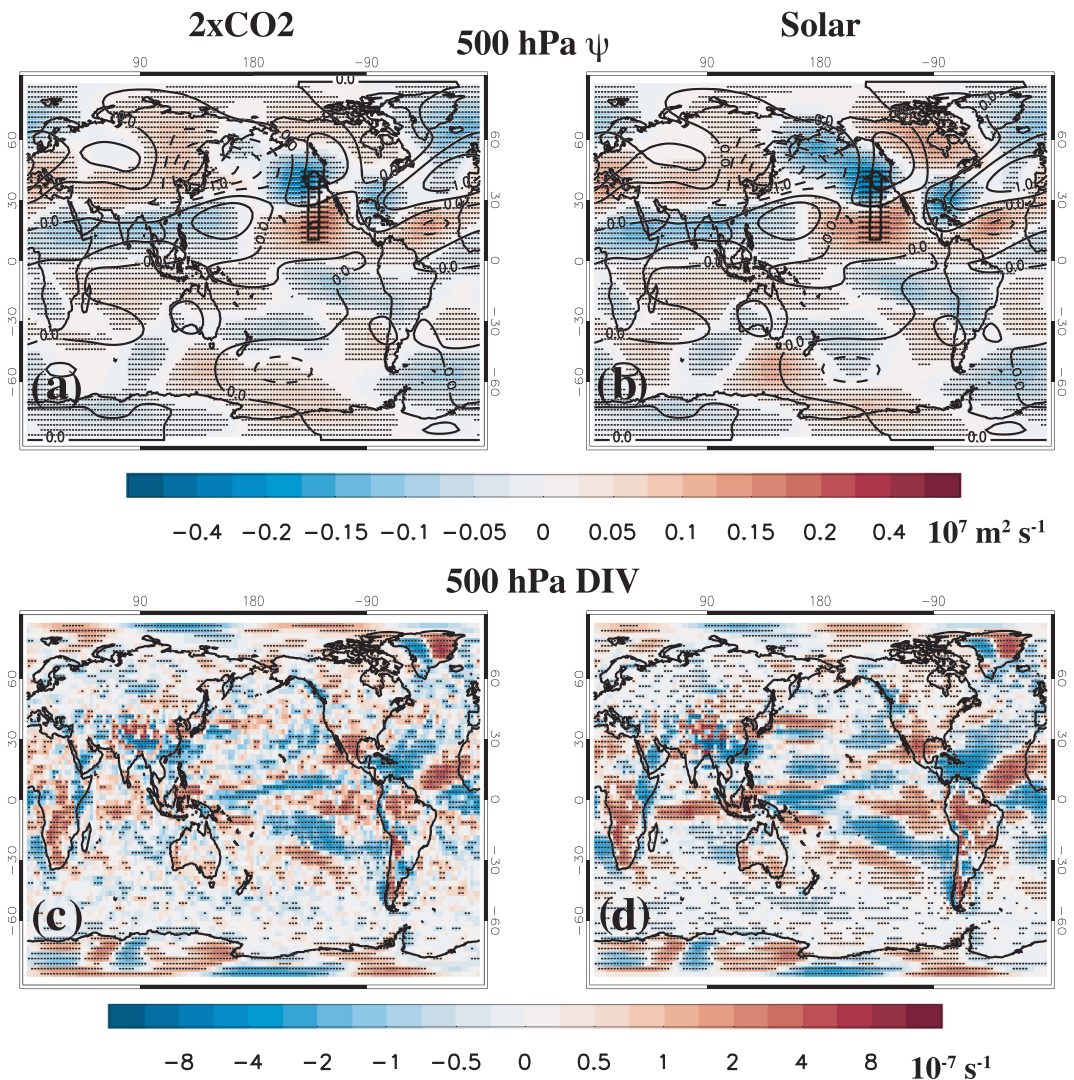


**Figure 10.** Wintertime ensemble mean 500-hPa stationary eddy stream function ( $\psi$ ) and divergence (DIV) response to (a, c) 2xCO<sub>2</sub> and (b, d) Solar+2%. Wintertime is defined as November through March. Changes significant at the 90% confidence level are denoted by black dots, based on a  $t$  test for the difference of means using the pooled variance. Climatological wintertime 500-hPa  $\psi$  in panels (a) and (b) are included as thin black contour lines, with negative values indicated by dashed lines. Black arrows in panels (a) and (b) sketch the direction in which the Rossby wave propagates in the Northern Hemisphere.  $\psi$  units are  $10^7 \text{ m}^2 \text{ s}^{-1}$ ; DIV units are  $10^{-7} \text{ s}^{-1}$ .

#### 4. Discussion

Similar to the results presented here, others have also found an increase in U.S. West Coast wintertime precipitation, including California, in response to increasing GHGs (Allen & Luptowitz, 2017; Chang et al., 2015; Neelin et al., 2013; Simpson et al., 2015). Simpson et al. (2015) associated these precipitation changes to changes in the stationary wave field that brings wetting southerlies to the West Coast of North America (and drying northerlies to interior southwest North America). This change in the meridional wind field is caused by strengthened zonal mean westerlies in the subtropical upper troposphere, which alters the character of intermediate-scale stationary waves. El Niño Southern Oscillation (ENSO) may also play a role, as model projections feature a shift to a more El Niño-like tropical Pacific background state (Cai et al., 2015), which may favor wetter winters for California (Allen & Luptowitz, 2017; Zecca et al., 2018). Increasing GHGs yield dynamically coherent tropical and extratropical responses in CMIP5 models that are reminiscent of an El Niño-like teleconnection, including an increase in eastern tropical Pacific divergence and a poleward propagating Rossby wave, and a southeastward shift of the upper level winds and an increase in storm track activity in the east Pacific. In addition to the extratropical wind response (Figures 5 and 6), we also find an

increase in eastern tropical Pacific divergence and a poleward Rossby wave response in  $2\times\text{CO}_2$  and Solar+2% (Figure 10). Models, however, may not be able to accurately simulate the tropical Pacific SST response to GHGs due to a cold bias of their equatorial cold tongues (Seager et al., 2019).

The poleward jet shift in response to BC is consistent with recent work (Allen et al., 2012b; Kovilakam & Mahajan, 2015; Shen & Ming, 2018). Allen et al. (2012b) showed that late 20th century trends in BC burden peak near the Northern Hemisphere (NH) midlatitudes, which preferentially warms the atmosphere there and decreases (increases) the baroclinicity on the equatorward (poleward) flank of the jet. This poleward shift of the latitude of maximum baroclinicity, by thermal wind balance, implies a corresponding poleward shift of the jet. A poleward jet shift also occurred in idealized simulations when a heating source was added to the midlatitude ( $30\text{--}60^\circ$ ) atmosphere (Allen et al., 2012a), as well as in response to future aerosol reductions (Allen & Ajoku, 2016). However, an equatorward jet shift occurred when heating was added to the high latitudes ( $60\text{--}90^\circ$ ) alone. Adding heat to the midlatitude and high-latitude ( $30\text{--}90^\circ$ ) atmosphere led to a weak poleward jet shift (Allen et al., 2012a). Thus, the jet shift depends on the location of the heating, with the largest poleward shift occurring in response to midlatitude heating (due to the aforementioned change in baroclinicity). More recently, Shen and Ming (2018) showed that the poleward jet shift in response to BC is due to the increase in midlatitude tropospheric stability, which results in less energetic baroclinic eddies and therefore reduced meridional energy transport in the midlatitudes.

Figure 11 shows the ensemble mean zonal mean ERF and tropospheric (850–300 hPa) temperature and zonal wind response for  $10\times\text{BC}$ , as well as the other climate drivers. Consistent with these prior studies,  $10\times\text{BC}$  features an NH lower-latitude to midlatitude ( $10\text{--}30\text{N}$ ) ERF maximum, as well as an NH midlatitude ( $\sim 40\text{N}$ ) peak in the tropospheric temperature response. There is also a reduction in the tropospheric zonal winds on the equatorward flank ( $20\text{--}40\text{N}$ ) of the climatological jet maximum (thin black lines) and a corresponding increase on the jet's poleward flank ( $50\text{--}70\text{N}$ ). This response implies a poleward shift of the tropospheric jet. Consistent with the large Asian contribution of BC to global emissions, similar results are obtained with  $10\times\text{BC}$  Asia. Interestingly, both BC responses also suggest a poleward jet displacement in the Southern Hemisphere, despite minimal forcing there.

The opposing PDRMIP jet shifts between sulfate and black carbon are similar to those reported in Allen and Sherwood (2011), where natural aerosols (mostly reflecting) led to an equatorward jet shift and anthropogenic aerosols (more absorbing) led to a poleward jet shift. Aerosol-induced cooling has also been shown to drive an equatorward jet shift in other studies (Fischer-Bruns et al., 2009; Ming & Ramaswamy, 2009; Ming et al., 2011). Aerosol cooling enhances the meridional temperature gradient equatorward of the NH jet but weakens it poleward, resulting in an equatorward jet shift. Aerosol-induced cooling was also found to displace the Aleutian low southeastward, which was accompanied by an equatorward displacement of the North Pacific jet and storm track (Ming et al., 2011). This was linked to stationary Rossby waves excited by the anomalous diabatic heating over the tropical east Pacific. Figure 11 shows that the sulfate simulations lead to an ERF minimum near  $20\text{--}40\text{N}$ , a weaker relative minimum in the tropospheric temperature response just poleward of the ERF minimum, and an increase (decrease) in the tropospheric zonal winds on the equatorward (poleward) flank of the climatological jet maximum. This response implies an equatorward shift of the tropospheric jet.

An interesting distinction between the aerosol and GHG 850–300-hPa NH zonal wind response is that the aerosol jet shift is relatively zonally uniform (e.g., Figure 11), whereas the GHG response is not. This is despite the more zonally asymmetric (symmetric) aerosol (GHG) forcing, particularly in the case of the regional aerosol simulations. In fact, the equatorward jet shift due to GHGs (and Solar+2%) primarily exists in the east Pacific (Figure 6), off the coast of California; the rest of the Pacific features a poleward jet shift, consistent with increased subtropical static stability and tropopause height (Allen et al., 2012a; Chen et al., 2008; Frierson et al., 2007; Lu et al., 2008; Lorenz & DeWeaver, 2007; Yin, 2005), leaving negligible shift of the NH jet in the zonal mean (Figure 11f). This zonal asymmetry in the NH jet shift in response to GHGs and Solar+2% further supports the role of Rossby waves, which are excited by the asymmetric change in tropical Pacific divergence (Figure 10). Future PDRMIP analyses will focus more specifically on how these climate drivers impact the tropical and extratropical atmospheric circulation, including the midlatitude jets and Hadley circulation.

Shen and Ming (2018) recently showed that the ability of BC to alter atmospheric circulation, including the poleward jet shift, increases with the altitude of BC. Significant differences exist between simulated profiles



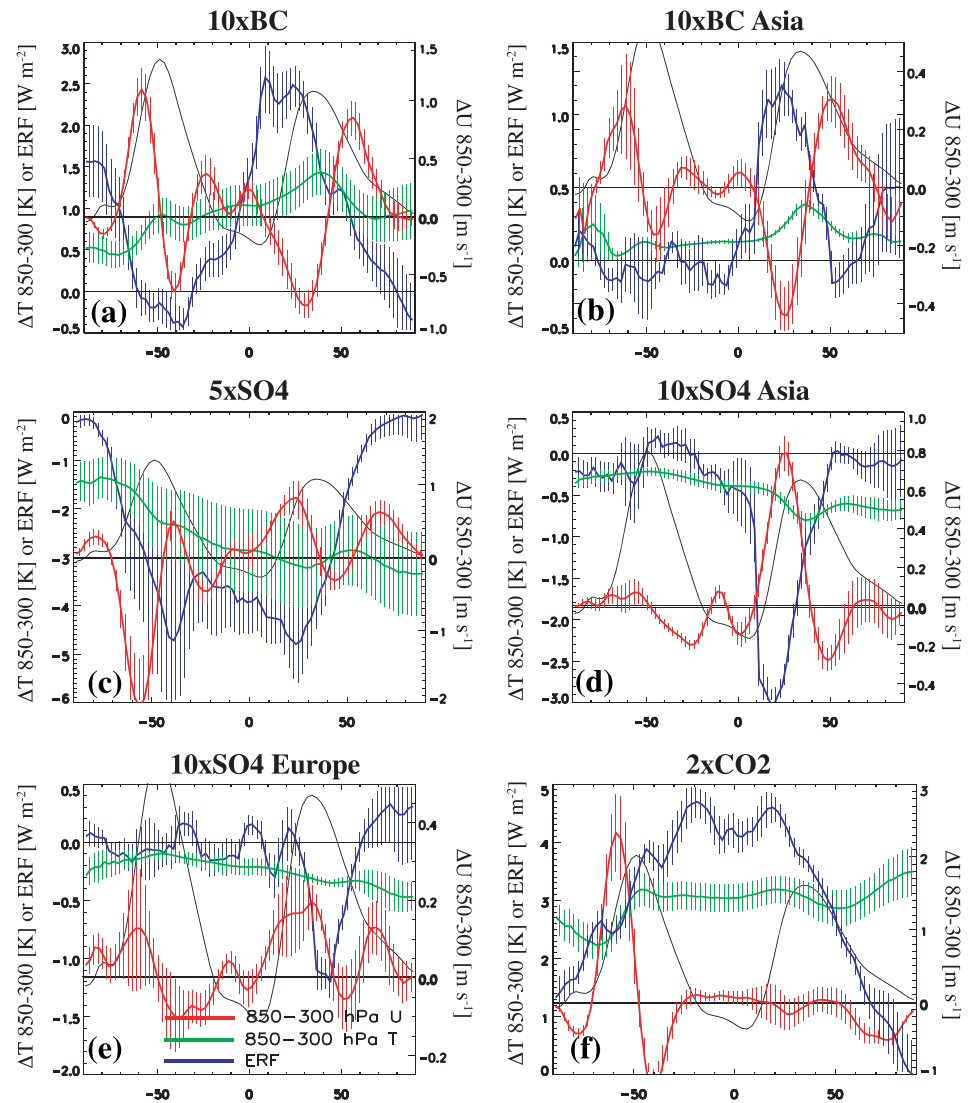


**Figure 11.** Wintertime ensemble mean zonal mean effective radiative forcing (ERF; blue) and tropospheric (850–300 hPa) temperature (T; green) and zonal wind (U; red) response to (a) 10xBC; (b) 10xBC Asia; (c) 5xSO<sub>4</sub>; (d) 10xSO<sub>4</sub> Asia; (e) 10xSO<sub>4</sub> Europe; and (f) 2xCO<sub>2</sub>. Thin vertical cross hatching indicates the standard error of the response, estimated as  $\sigma/\sqrt{n}$ , where  $\sigma$  is the intermodel standard deviation and  $n$  is the number of models. Note that panels have different scalings of the y axes. Thin black lines show the wintertime climatological U 850–300 hPa (i.e., tropospheric jet), scaled by 1/10 for 2xCO<sub>2</sub>; 1/15 for 10xBC and 5xSO<sub>4</sub>; 1/25 for 10xSO<sub>4</sub> Asia; and 1/35 for 10xSO<sub>4</sub> Europe and 10xBC Asia. ERF units are W m<sup>-2</sup>; 850–300-hPa temperature units are K; and 850–300-hPa U units are m s<sup>-1</sup>.

of the vertical BC distribution (Koch et al., 2009; Textor et al., 2006, 2007), with climate models likely having too much BC in the upper troposphere/stratosphere (Allen & Landuyt, 2014). Causes remain uncertain but are thought to be related to wet removal (Kipling et al., 2013), convective transport (Allen & Landuyt, 2014; Park & Allen, 2015; Storelvmo, 2012), injection height (Labonne et al., 2007), and/or physical aging (Liu et al., 2011). Allen et al. (2019) showed that PDRMIP models overestimate the amount of BC atmospheric heating relative to a semiempirical estimate (Chung et al., 2016) constrained by a suite of aerosol observations, including the vertical aerosol profile from the Cloud-Aerosol Lidar with Orthogonal Polarization (CALIOP) (Winker et al., 2009). This in turn was linked to significant differences in the rapid adjustment, including clouds, surface temperature, and precipitation. This suggests the PDRMIP BC jet response may be too strong and highlights the importance of improved constraints on the simulated aerosol vertical profile. This will be evaluated during Phase 2 of PDRMIP, in which 10xBC simulations with a shortened lifetime (~3 days, as opposed to the current multimodel mean of 9.64 days Stjern et al., 2017) will be conducted.



The experimental design of PDRMIP is idealized, which makes a formal attribution difficult. This is particularly true in the case of aerosols, where emissions have varied both spatially and temporally, which is not accounted for in PDRMIP simulations. Aerosol emissions from Europe and North America peaked in the late 1970s and have since declined substantially due to air pollution controls and clean air regulations (Allen et al., 2013; Lamarque et al., 2010; Streets et al., 2009; Wild, 2012). In contrast, aerosol emissions from Asia and India were just starting to ramp up in the late 20th century and now dominate global aerosol emissions. China, however, has recently implemented sulfur dioxide emission controls, resulting in a 75% reduction in sulfate aerosol since 2007 (Li et al., 2017). The PDRMIP regional aerosol simulations highlight the location-dependent climate response of aerosol, which does not simply scale with the global mean ERF (e.g., Figure 9). Another difficulty in using PDRMIP idealized simulations for a formal attribution is the possibility of nonlinear climate responses to aerosol forcing (Feichter et al., 2004; Ming & Ramaswamy, 2009), including dependence on the background aerosol state (Carslaw et al., 2017).

## 5. Conclusions

Using model simulations from PDRMIP, we have quantified how various climate drivers affect winter-time precipitation along the U.S. West Coast, focused on California. Consistent with recent work (Allen & Luptowitz, 2017; Neelin et al., 2013), GHGs including both CO<sub>2</sub> and CH<sub>4</sub>, as well as solar forcing, drive a robust increase in California wintertime precipitation. We also find robust California precipitation responses to atmospheric aerosol forcing but with near opposite responses for absorbing (BC) versus reflecting (sulfate) aerosol. BC leads to a decrease in California precipitation, whereas sulfate leads to an increase. This wetting is particularly strong for both European and Asian sulfate.

Although a formal attribution is not possible with PDRMIP simulations, our results suggest aerosols can perturb California precipitation and that they may be important drivers of California precipitation change. This is particularly relevant over the next several decades, as aerosol emissions are expected to rapidly decline (Gidden et al., 2019). Interestingly, the offsetting tendencies of absorbing versus reflecting aerosols, combined with the relatively large natural variability of California precipitation (Deser et al., 2012), may make detection of an aerosol impact difficult. More detailed transient simulations with (and without) temporally and spatially varying aerosol emissions and precursor gases would be required to formally attribute California precipitation changes to atmospheric aerosols. Simulations currently being conducted in support of CMIP6, under the Aerosol Chemistry Model Intercomparison Project (AerChemMIP) (Collins et al., 2017) feature such 20th century transient simulations, including future projections driven by emission scenarios with weak versus strong air quality control measures, which would allow a formal attribution.

## Conflict of Interest

The authors declare no competing financial interests.

## Data Availability Statement

PDRMIP simulations can be accessed at <https://cicero.oslo.no/en/PDRMIP>.

## References

- Ackerley, D., Booth, B. B. B., Knight, S. H. E., Highwood, E. J., Frame, D. J., Allen, M. R., & Rowell, D. P. (2011). Sensitivity of twentieth-century Sahel rainfall to sulfate aerosol and CO<sub>2</sub> forcing. *Journal of Climate*, 24(19), 4999–5014. <https://doi.org/10.1175/JCLI-D-11-00019.1>
- Allen, R. J., & Ajoku, O. (2016). Future aerosol reduction and widening of the northern tropical belt. *Journal of Geophysical Research: Atmospheres*, 121, 6765–6786. <https://doi.org/10.1002/2016JD024803>
- Allen, R. J., & Anderson, R. G. (2018). 21st century California drought risk linked to model fidelity of the El Niño teleconnection. *NPJ Climate and Atmospheric Science*, 1(1), 21. <https://doi.org/10.1038/s41612-018-0032-x>
- Allen, R. J., Evan, A. T., & Booth, B. B. B. (2015). Interhemispheric aerosol radiative forcing and tropical precipitation shifts during the late twentieth century. *Journal of Climate*, 28(20), 8219–8246. <https://doi.org/10.1175/JCLI-D-15-0148.1>
- Allen, R. J., Hassan, T., Randles, C. A., & Su, H. (2019). Enhanced land-sea warming contrast elevates aerosol pollution in a warmer world. *Nature Climate Change*, 9, 300–305. <https://doi.org/10.1038/s41558-019-0401-4>
- Allen, R. J., & Landuyt, W. (2014). The vertical distribution of black carbon in CMIP5 models: Comparison to observations and the importance of convective transport. *Journal of Geophysical Research: Atmospheres*, 119, 4808–4835. <https://doi.org/10.1002/2014JD021595>
- Allen, R. J., Landuyt, W., & Rumbold, S. T. (2016). An increase in aerosol burden and radiative effects in a warmer world. *Nature Climate Change*, 6, 269–274. <https://doi.org/10.1038/nclimate2827>

## Acknowledgments

DWP receives funding from the European Union's Horizon 2020 research and innovation programme iMIRACLI under Marie Skłodowska-Curie grant agreement No 860100. DWP also gratefully acknowledges funding from the NERC ACRISE project NE/S005390/1.

- Allen, R. J., & Luptowitz, R. (2017). El Niño-like teleconnection increases California precipitation in response to warming. *Nature Communications*, 8, 16055 EP. <https://doi.org/10.1038/ncomms16055>
- Allen, R. J., Norris, J. R., & Wild, M. (2013). Evaluation of multidecadal variability in CMIP5 surface solar radiation and inferred underestimation of aerosol direct effects over Europe, China, Japan and India. *Journal of Geophysical Research: Atmospheres*, 118, 6311–6336. <https://doi.org/10.1002/jgrd.50426>
- Allen, R. J., & Sherwood, S. C. (2011). The impact of natural versus anthropogenic aerosols on atmospheric circulation in the Community Atmosphere Model. *Climate Dynamics*, 1959–1978. <https://doi.org/10.1007/s00382-010-0898-8>
- Allen, R. J., Sherwood, S. C., Norris, J. R., & Zender, C. S. (2012). The equilibrium response to idealized thermal forcings in a comprehensive GCM: Implications for recent tropical expansion. *Atmospheric Chemistry and Physics*, 12, 4795–4816. <https://doi.org/10.5194/acp-12-4795-2012>
- Allen, R. J., Sherwood, S. C., Norris, J. R., & Zender, C. S. (2012). Recent northern hemisphere tropical expansion primarily driven by black carbon and tropospheric ozone. *Nature*, 485, 350–354. <https://doi.org/10.1038/nature11097>
- Andrews, T., Forster, P. M., Boucher, O., Bellouin, N., & Jones, A. (2010). Precipitation, radiative forcing and global temperature change. *Geophysical Research Letters*, 37, L14701. <https://doi.org/10.1029/2010GL043991>
- Arora, V. K., Scinocca, J. F., Boer, G. J., Christian, J. R., Denman, K. L., Flato, G. M., & Merryfield, W. J. (2011). Carbon emission limits required to satisfy future representative concentration pathways of greenhouse gases. *Geophysical Research Letters*, 38, L05805. <https://doi.org/10.1029/2010GL046270>
- Bedsworth, L., Cayan, D. G. F., Fisher, L., & Ziaja, S. (2018). Statewide Summary Report. California's Fourth Climate Change Assessment: California Energy Commission, California Public Utilities Commission.
- Bellouin, N., Rae, J., Jones, A., Johnson, C., Haywood, J., & Boucher, O. (2011). Aerosol forcing in the Climate Model Intercomparison Project (CMIP5) simulations by HadGEM2-ES and the role of ammonium nitrate. *Journal of Geophysical Research*, D20, D20206. <https://doi.org/10.1029/2011JD016074>
- Bentsen, M., Bethke, I., Debernard, J. B., Iversen, T., Kirkevåg, A., Seland, Ø., & Kristjánsson, J. E. (2013). The Norwegian Earth System Model, NorESM1-M-Part 1: Description and basic evaluation of the physical climate. *Geoscientific Model Development*, 6(3), 687–720. <https://doi.org/10.5194/gmd-6-687-2013>
- Biasutti, M., & Giannini, A. (2006). Robust Sahel drying in response to late 20th century forcings. *Geophysical Research Letters*, 33, L11706. <https://doi.org/10.1029/2006GL026067>
- Cai, W., Santoso, A., Wang, G., Yeh, S. W., An, S. I., Cobb, K. M., & Wu, L. (2015). ENSO and greenhouse warming. *Nature Climate Change*, 5, 849–859. <https://doi.org/10.1038/nclimate2743>
- Carslaw, K. S., Gordon, H., Hamilton, D. S., Johnson, J. S., Regayre, L. A., Yoshioka, M., & Pringle, K. J. (2017). Aerosols in the pre-industrial atmosphere. *Current Climate Change Reports*, 3(1), 1–15. <https://doi.org/10.1007/s40641-017-0061-2>
- Cayan, D. R., Das, T., Pierce, D. W., Barnett, T. P., Tyree, M., & Gershunov, A. (2010). Future dryness in the southwest US and the hydrology of the early 21st century drought. *Proceedings of the National Academy of Sciences*, 107, 21,271–21,276. <https://doi.org/10.1073/pnas.0912391107>
- Chang, C. Y., Chiang, J. C. H., Wehner, M. F., Friedman, A. R., & Ruedy, R. (2011). Sulfate aerosol control of tropical atlantic climate over the twentieth century. *Journal of Climate*, 24(10), 2540–2555. <https://doi.org/10.1175/2010JCLI4065.1>
- Chang, E. K. M., Zheng, C., Lanigan, P., Yau, A. M. W., & Neelin, J. D. (2015). Significant modulation of variability and projected change in California winter precipitation by extratropical cyclone activity. *Geophysical Research Letters*, 42, 5983–5991. <https://doi.org/10.1002/2015GL064424>
- Chen, G., Lu, J., & Frierson, D. W. (2008). Phase speed spectra and the latitude of surface westerlies: Interannual variability and global warming trend. *Journal Climate*, 21, 5942–5959.
- Chung, C. E., Chu, J. E., Lee, Y., van Noije, T., Jeoung, H., Ha, K. J., & Marks, M. (2016). Global fine-mode aerosol radiative effect, as constrained by comprehensive observations. *Atmospheric Chemistry and Physics*, 16(13), 8071–8080. <https://doi.org/10.5194/acp-16-8071-2016>
- Collins, W. J., Bellouin, N., Doutriaux-Boucher, M., Gedney, N., Halloran, P., Hinton, T., & Woodward, S. (2011). Development and evaluation of an Earth-system model—HadGEM2. *Geoscientific Model Development*, 4(4), 1051–1075. <https://doi.org/10.5194/gmd-4-1051-2011>
- Collins, M., Knutti, R., Arblaster, J., Dufresne, J. L., Fichet, T., Friedlingstein, P., & Wehner, M. (2013). Long-term climate change: Projections, commitments and irreversibility. In T. Stocker (Ed.), *Climate Change 2013: The Physical Science Basis. Contribution of Working Group I to the Fifth Assessment Report of the Intergovernmental Panel on Climate Change* (pp. 1029–1136). Cambridge, United Kingdom, and New York, NY: Cambridge University Press.
- Collins, W. J., Lamarque, J. F., Schulz, M., Boucher, O., Eyring, V., Hegglin, M. I., & Smith, S. J. (2017). AerChemMIP: Quantifying the effects of chemistry and aerosols in CMIP6. *Geoscientific Model Development*, 10(2), 585–607. <https://doi.org/10.5194/gmd-10-585-2017>
- Cook, B. I., Ault, T. R., & Smerdon, J. E. (2015). Unprecedented 21st century drought risk in the American Southwest and Central Plains. *Science Advances*, 1, e1400082. <https://doi.org/10.1126/sciadv.1400082>
- Cubasch, U., Wuebbles, D., Chen, D., Facchini, M. C., Frame, D., Mahowald, N., & Winther, J. G. (2013). Introduction. In T. F. Stocker et al. (Eds.), *Climate Change 2013: The Physical Science Basis. Contribution of Working Group I to the Fifth Assessment Report of the Intergovernmental Panel on Climate Change* (pp. 119–158). Cambridge, United Kingdom and New York, NY, USA: Cambridge University Press.
- Deser, C., Knutti, R., Solomon, S., & Phillips, A. S. (2012). Communication of the role of natural variability in future North American climate. *Nature Climate Change*, 2, 775–779. <https://doi.org/10.1038/nclimate1562>
- Dettinger, M. D. (2011). Climate change, atmospheric rivers and floods in California—A multimodel analysis of storm frequency and magnitude changes. *Journal of American Water Resources Association*, 47(3), 514–523. <https://doi.org/10.1111/j.1752-1688.2011.00546.x>
- Diffenbaugh, N. S., Swain, D. L., & Touma, D. (2015). Anthropogenic warming has increased drought risk in California. *Proceedings of the National Academy of Sciences*, 112, 3931–3936. <https://doi.org/10.1073/pnas.1422385112>
- Dufresne, J. L., Foujols, M. A., Denvil, S., Caubel, A., Marti, O., Aumont, O., & Vuichard, N. (2013). Climate change projections using the IPSL-CM5 Earth System Model: from CMIP3 to CMIP5. *Climate Dynamics*, 40(9), 2123–2165. <https://doi.org/10.1007/s00382-012-1636-1>
- Feichter, J., Roeckner, E., Lohmann, U., & Liepert, B. (2004). Nonlinear aspects of the climate response to greenhouse gas and aerosol forcing. *Journal of Climate*, 17(12), 2384–2398. [https://doi.org/10.1175/1520-0442\(2004\)017<2384:NAOTCR>2.0.CO;2](https://doi.org/10.1175/1520-0442(2004)017<2384:NAOTCR>2.0.CO;2)
- Fischer-Bruns, I., Banse, D. F., & Feichter, J. (2009). Future impact of anthropogenic sulfate aerosol on North Atlantic climate. *Climate Dynamics*, 32(4), 511–524. <https://doi.org/10.1007/s00382-008-0458-7>

- Forster, P. M., Richardson, T., Maycock, A. C., Smith, C. J., Samset, B. H., Myhre, G., & Schulz, M. (2016). Recommendations for diagnosing effective radiative forcing from climate models for CMIP6. *Journal of Geophysical Research: Atmospheres*, 121, 12,460–12,475. <https://doi.org/10.1002/2016JD025320>
- Frierson, D. M. W., & Hwang, Y. T. (2012). Extratropical influence on ITCZ shifts in slab ocean simulations of global warming. *Journal of Climate*, 25(2), 720–733. <https://doi.org/10.1175/JCLI-D-11-00116.1>
- Frierson, D. M. W., Lu, J., & Chen, G. (2007). Width of the Hadley cell in simple and comprehensive general circulation models. *Geophysical Research Letters*, 34, L18804. <https://doi.org/10.1029/2007GL031115>
- Gao, Y., Leung, L. R., Lu, J., Liu, Y., Huang, M., & Qian, Y. (2014). Robust spring drying in the southwestern U.S. and seasonal migration of wet/dry patterns in a warmer climate. *Geophysical Research Letters*, 41, 1745–1751. <https://doi.org/10.1002/2014GL059562>
- Gidden, M. J., Riahi, K., Smith, S. J., Fujimori, S., Luderer, G., Kriegler, E., & Takahashi, K. (2019). Global emissions pathways under different socioeconomic scenarios for use in CMIP6: A dataset of harmonized emissions trajectories through the end of the century. *Geoscientific Model Development*, 12(4), 1443–1475. <https://doi.org/10.5194/gmd-12-1443-2019>
- Hagos, S. M., Leung, L. R., Yoon, J. H., Lu, J., & Gao, Y. (2016). A projection of changes in landfalling atmospheric river frequency and extreme precipitation over western North America from the Large Ensemble CESM simulations. *Geophysical Research Letters*, 43, 1357–1363. <https://doi.org/10.1002/2015GL067392>
- Held, I. M., & Soden, B. J. (2006). Robust responses of the hydrological cycle to global warming. *Journal of Climate*, 19, 5686–5699.
- Hoerling, M., Eischeid, J., Perlwitz, J., Quan, X., Zhang, T., & Pegion, P. (2012). On the increased frequency of Mediterranean drought. *Journal of Climate*, 25(6), 2146–2161. <https://doi.org/10.1175/JCLI-D-11-00296.1>
- Hurrell, J. W., Holland, M. M., Gent, P. R., Ghan, S., Kay, J. E., Kushner, P. J., & Marshall, S. (2013). The Community Earth System Model: A framework for collaborative research. *Bulletin of the American Meteorological Society*, 94(9), 1339–1360. <https://doi.org/10.1175/BAMS-D-12-00121.1>
- Hwang, Y. T., Frierson, D. M. W., & Kang, S. M. (2013). Anthropogenic sulfate aerosol and the southward shift of tropical precipitation in the late 20th century. *Geophysical Research Letters*, 40(11), 2845–2850. <https://doi.org/10.1002/grl.50502>
- Kipling, Z., Stier, P., Schwarz, J. P., Perring, A. E., Spackman, J. R., Mann, G. W., & Telford, P. J. (2013). Constraints on aerosol processes in climate models from vertically-resolved aircraft observations of black carbon. *Atmospheric Chemistry and Physics*, 13(12), 5969–5986. <https://doi.org/10.5194/acp-13-5969-2013>
- Koch, D., Schulz, M., Kinne, S., McNaughton, C., Spackman, J. R., Balkanski, Y., & Zhao, Y. (2009). Evaluation of black carbon estimations in global aerosol models. *Atmospheric Chemistry and Physics*, 9(22), 9001–9026.
- Kovilakam, M., & Mahajan, S. (2015). Black carbon aerosol-induced Northern Hemisphere tropical expansion. *Geophysical Research Letters*, 42, 4964–4972. <https://doi.org/10.1002/2015GL064559>
- Krishnan, R., Sabin, T. P., Vellore, R., Mujumdar, M., Sanjay, J., Goswami, B. N., & Terray, P. (2016). Deciphering the desiccation trend of the South Asian monsoon hydroclimate in a warming world. *Climate Dynamics*, 47(3), 1007–1027. <https://doi.org/10.1007/s00382-015-2886-5>
- Labonne, M., Bréon, F. M., & Chevallier, F. (2007). Injection height of biomass burning aerosols as seen from a spaceborne lidar. *Geophysical Research Letters*, 34, L11806. <https://doi.org/10.1029/2007GL029311>
- Lamarque, J. F., Bond, T. C., Eyring, V., Granier, C., Heil, A., Klimont, Z., & van Vuuren, D. P. (2010). Historical (1850–2000) gridded anthropogenic and biomass burning emissions of reactive gases and aerosols: Methodology and application. *Atmospheric Chemistry and Physics*, 10, 7017–7039. <https://doi.org/10.5194/acp-10-7017-2010>
- Lau, W. K. M., & Kim, K. M. (2017). Competing influences of greenhouse warming and aerosols on Asian summer monsoon circulation and rainfall. *Asia-Pacific Journal of Atmospheric Sciences*, 53(2), 181–194. <https://doi.org/10.1007/s13143-017-0033-4>
- Lavers, D. A., Ralph, F. M., Waliser, D. E., Gershunov, A., & Dettinger, M. D. (2015). Climate change intensification of horizontal water vapor transport in CMIP5. *Geophysical Research Letters*, 42, 5617–5625. <https://doi.org/10.1002/2015GL064672>
- Li, C., McLinden, C., Fioletov, V., Krotkov, N., Carn, S., Joiner, J., & Dickerson, R. R. (2017). India is overtaking China as the world's largest emitter of anthropogenic sulfur dioxide. *Scientific Reports*, 7(1), 14,304. <https://doi.org/10.1038/s41598-017-14639-8>
- Li, X., Ting, M., Li, C., & Henderson, N. (2015). Mechanisms of Asian summer monsoon changes in response to anthropogenic forcing in CMIP5 models. *Journal of Climate*, 28(10), 4107–4125. <https://doi.org/10.1175/JCLI-D-14-00559.1>
- Liepert, B. G., Feichter, J., Lohmann, U., & Roeckner, E. (2004). Can aerosols spin down the water cycle in a warmer and moister world? *Geophysical Research Letters*, 31, L06207. <https://doi.org/10.1029/2003GL019060>
- Liepert, B. G., & Previdi, M. (2009). Do models and observations disagree on the rainfall response to global warming? *Journal of Climate*, 22, 3156–3166.
- Lin, L., Xu, Y., Wang, Z., Diao, C., Dong, W., & Xie, S. P. (2018). Changes in extreme rainfall over India and China attributed to regional aerosol-cloud interaction during the late 20th century rapid industrialization. *Geophysical Research Letters*, 45, 7857–7865. <https://doi.org/10.1029/2018GL078308>
- Liu, J., Fan, S., Horowitz, L. W., & Levy, H. (2011). Evaluation of factors controlling long-range transport of black carbon to the Arctic. *Journal of Geophysical Research*, 116, D04307. <https://doi.org/10.1029/2010JD015145>
- Liu, L., Shawki, D., Voulgarakis, A., Kasoar, M., Samset, B. H., Myhre, G., & Takemura, T. (2018). A PDRMIP multimodel study on the impacts of regional aerosol forcings on global and regional precipitation. *Journal of Climate*, 31(11), 4429–4447. <https://doi.org/10.1175/JCLI-D-17-0439.1>
- Lorenz, D. J., & DeWeaver, E. T. (2007). Tropopause height and zonal wind response to global warming in the IPCC scenario integrations. *Journal of Geophysical Research*, 112, D10119. <https://doi.org/10.1029/2006JD008087>
- Lu, J., Chen, G., & Frierson, D. M. W. (2008). Response of the zonal mean atmospheric circulation to El Niño versus global warming. *Journal of Climate*, 21, 5835–5851.
- Meehl, G. A., Stocker, T. F., Collins, W. D., Friedlingstein, P., Gaye, A. T., Gregory, J. M., et al. (2007). Global climate projections. In S. Iomom (Ed.), *Climate Change 2007: The Physical Science Basis. Contribution of Working Group I to the Fourth Assessment Report of the Intergovernmental Panel on Climate Change* (pp. 747–846). Cambridge, United Kingdom, and New York, NY: Cambridge University Press.
- Ming, Y., & Ramaswamy, V. (2009). Nonlinear climate and hydrological responses to aerosol effects. *Journal of Climate*, 22(6), 13,290–13,339. <https://doi.org/10.1175/2008JCLI2362.1>
- Ming, Y., Ramaswamy, V., & Chen, G. (2011). A model investigation of aerosol-induced changes in boreal winter extratropical circulation. *Journal of Climate*, 24, 6077–6091. <https://doi.org/10.1175/2011JCLI4111.1>
- Myhre, G., Forster, P. M., Samset, B. H., Hodnebrog, Ø., Sillmann, J., Aalbergsjø, S. G., & Zwiers, F. (2017). PDRMIP: A Precipitation Driver and Response Model Intercomparison Project—Protocol and preliminary results. *Bulletin of the American Meteorological Society*, 98(6), 1185–1198. <https://doi.org/10.1175/BAMS-D-16-0019.1>

- Neale, R. B., Richter, J. H., Conley, A. J., Park, S., Lauritzen, P. H., Gettelman, A., & Lin, S. J. (2010). Description of the NCAR Community Atmosphere Model (CAM 4.0): National Center for Atmospheric Research.
- Neelin, J. D., Langenbrunner, B., Meyerson, J. E., Hall, A., & Berg, N. (2013). California winter precipitation change under global warming in the Coupled Model Intercomparison Project phase 5 ensemble. *Journal of Climate*, 26, 6238–6256. <https://doi.org/10.1175/JCLI-D-12-00514.1>
- Park, S., & Allen, R. J. (2015). Understanding influences of convective transport and removal processes on aerosol vertical distribution. *Geophysical Research Letters*, 42, 10,438–10,444. <https://doi.org/10.1002/2015GL066175>
- Payne, A. E., & Magnusdottir, G. (2015). An evaluation of atmospheric rivers over the North Pacific in CMIP5 and their response to warming under RCP8.5. *Journal of Geophysical Research: Atmospheres*, 120, 11,173–11,190. <https://doi.org/10.1002/2015JD023586>
- Polade, S. D., Gershunov, A., Cayan, D. R., Dettinger, M. D., & Pierce, D. W. (2017). Precipitation in a warming world: Assessing projected hydro-climate changes in California and other Mediterranean climate regions. *Scientific Reports*, 7(1), 10,783. <https://doi.org/10.1038/s41598-017-11285-y>
- Richardson, T. B., Forster, P. M., Andrews, T., Boucher, O., Faluvegi, G., Fläschner, D., & Voulgarakis, A. (2018). Drivers of precipitation change: An energetic understanding. *Journal of Climate*, 31(23), 9641–9657. <https://doi.org/10.1175/JCLI-D-17-0240.1>
- Salzmann, M. (2016). Global warming without global mean precipitation increase? *Science Advances*, 2(6), e1501572. <https://doi.org/10.1126/sciadv.1501572>
- Samset, B. H., Myhre, G., Forster, P. M., Hodnebrog, Ø., Andrews, T., Faluvegi, G., & Voulgarakis, A. (2016). Fast and slow precipitation responses to individual climate forcers: A PDRMIP multimodel study. *Geophysical Research Letters*, 43, 2782–2791. <https://doi.org/10.1002/2016GL068064>
- Sand, M., Iversen, T., Bohlinger, P., Kirkevåg, A., Seierstad, I., Seland, Ø., & Sorteberg, A. (2015). A standardized global climate model study showing unique properties for the climate response to black carbon aerosols. *Journal of Climate*, 28(6), 2512–2526. <https://doi.org/10.1175/JCLI-D-14-00050.1>
- Schmidt, G. A., Kelley, M., Nazarenko, L., Ruedy, R., Russell, G. L., Aleinov, I., & Zhang, J. (2014). Configuration and assessment of the GISS ModelE2 contributions to the CMIP5 archive. *Journal of Advances in Modeling Earth Systems*, 6, 141–184. <https://doi.org/10.1002/2013MS000265>
- Seager, R., Cane, M., Henderson, N., Lee, D. E., Abernathey, R., & Zhang, H. (2019). Strengthening tropical Pacific zonal sea surface temperature gradient consistent with rising greenhouse gases. *Nature Climate Change*, 9(7), 517–522. <https://doi.org/10.1038/s41558-019-0505-x>
- Seager, R., Naik, N., & Vecchi, G. A. (2010). Thermodynamic and dynamic mechanisms for large-scale changes in the hydrological cycle in response to global warming. *Journal of Climate*, 23, 4651–4668. <https://doi.org/10.1175/2010JCLI3655.1>
- Seager, R., Neelin, D., Simpson, I., Liu, H., Henderson, N., Shaw, T., & Cook, B. (2014). Dynamical and thermodynamical causes of large-scale changes in the hydrological cycle over North America in response to global warming. *Journal of Climate*, 27, 7921–7948. <https://doi.org/10.1175/JCLI-D-14-00153.1>
- Shen, Z., & Ming, Y. (2018). The influence of aerosol absorption on the extratropical circulation. *Journal of Climate*, 31(15), 5961–5975. <https://doi.org/10.1175/JCLI-D-17-0839.1>
- Simpson, I. R., Seager, R., Ting, M., & Shaw, T. A. (2015). Causes of change in Northern Hemisphere winter meridional winds and regional hydroclimate. *Nature Climate Change*, 6, 65–70. <https://doi.org/10.1038/nclimate2783>
- Stjern, C. W., Samset, B. H., Myhre, G., Forster, P. M., Hodnebrog, Ø., Andrews, T., & Voulgarakis, A. (2017). Rapid adjustments cause weak surface temperature response to increased black carbon concentrations. *Journal of Geophysical Research: Atmospheres*, 122, 11,462–11,481. <https://doi.org/10.1002/2017JD027326>
- Storelvmo, T. (2012). Uncertainties in aerosol direct and indirect effects attributed to uncertainties in convective transport mechanisms. *Atmospheric Research*, 118, 357–369. <https://doi.org/10.1016/j.atmosres.2012.06.022>
- Streets, D. G., Yan, F., Chin, M., Diehl, T., Mahowald, N., Schultz, M., & Yu, C. (2009). Anthropogenic and natural contributions to regional trends in aerosol optical depth, 1980–2006. *Journal of Geophysical Research*, 114, D00D18. <https://doi.org/10.1029/2008JD011624>
- Swain, D. L., Langenbrunner, B., Neelin, J. D., & Hall, A. (2018). Increasing precipitation volatility in twenty-first-century California. *Nature Climate Change*, 8(6), 427–433. <https://doi.org/10.1038/s41558-018-0140-y>
- Takemura, T., Egashira, M., Matsuzawa, K., Ichijo, H., Oishi, R., & Abe-Ouchi, A. (2009). A simulation of the global distribution and radiative forcing of soil dust aerosols at the Last Glacial Maximum. *Atmospheric Chemistry and Physics*, 9(9), 3061–3073. <https://doi.org/10.5194/acp-9-3061-2009>
- Takemura, T., Nozawa, T., Emori, S., Nakajima, T. Y., & Nakajima, T. (2005). Simulation of climate response to aerosol direct and indirect effects with aerosol transport-radiation model. *Journal of Geophysical Research: Atmospheres*, 110(D2), D02202. <https://doi.org/10.1029/2004JD005029>
- Tang, T., Shindell, D., Samset, B. H., Boucher, O., Forster, P. M., Hodnebrog, Ø., & Takemura, T. (2018). Dynamical response of Mediterranean precipitation to greenhouse gases and aerosols. *Atmospheric Chemistry and Physics*, 18(11), 8439–8452. <https://doi.org/10.5194/acp-18-8439-2018>
- Taylor, K. E., Stouffer, R. J., & Meehl, G. A. (2012). An overview of CMIP5 and the experiment design. *Bulletin of the American Meteorological Society*, 93, 485–498.
- Textor, C., Schulz, M., Guibert, S., Kinne, S., Balkanski, Y., Bauer, S., & Tie, X. (2006). Analysis and quantification of the diversities of aerosol life cycles within AeroCom. *Atmospheric Chemistry and Physics*, 6, 1777–1813. <https://doi.org/10.5194/acp-6-1777-2006>
- Textor, C., Schulz, M., Guibert, S., Kinne, S., Balkanski, Y., Bauer, S., & Tie, X. (2007). The effect of harmonized emissions on aerosol properties in global models—An AeroCom experiment. *Atmospheric Chemistry and Physics*, 7(17), 4489–4501. <https://doi.org/10.5194/acp-7-4489-2007>
- Trenberth, K. E., & Guillemot, C. J. (1995). Evaluation of the global atmospheric moisture budget as seen from analyses. *Journal of Climate*, 8, 2255–2272. [https://doi.org/10.1175/1520-0442\(1995\)008<2255:EOTGAM>2.0.CO;2](https://doi.org/10.1175/1520-0442(1995)008<2255:EOTGAM>2.0.CO;2)
- Undorf, S., Polson, D., Bollasina, M. A., Ming, Y., Schurer, A., & Hegerl, G. C. (2018). Detectable impact of local and remote anthropogenic aerosols on the 20th century changes of West African and South Asian monsoon precipitation. *Journal of Geophysical Research: Atmospheres*, 123, 4871–4889. <https://doi.org/10.1029/2017JD027711>
- Wild, M. (2012). Enlightening global dimming and brightening. *Bulletin of the American Meteorological Society*, 93, 27–37. <https://doi.org/10.1175/BAMS-D-11-00074.1>
- Winker, D. M., Vaughan, M. A., Omar, A., Hu, Y., Powell, K. A., Liu, Z., & Young, S. A. (2009). Overview of the CALIPSO Mission and CALIOP data processing algorithms. *Journal of Atmospheric and Oceanic Technology*, 26(11), 2310–2323. <https://doi.org/10.1175/2009JTECHA1281.1>

- Wu, P., Christidis, N., & Stott, P. (2013). Anthropogenic impact on Earth's hydrological cycle. *Nature Climate Change*, 3, 807 EP-. <https://doi.org/10.1038/nclimate1932>
- Yin, J. H. (2005). A consistent poleward shift of the storm tracks in simulations of 21st century climate. *Geophysical Research Letters*, 32, L18701. <https://doi.org/10.1029/2005GL023684>
- Zecca, K., Allen, R. J., & Anderson, R. G. (2018). Importance of the El Niño teleconnection to the 21st century California wintertime extreme precipitation increase. *Geophysical Research Letters*, 45, 10,648–10,655. <https://doi.org/10.1029/2018GL079714>
- Zhang, K., O'Donnell, D., Kazil, J., Stier, P., Kinne, S., Lohmann, U., & Feichter, J. (2012). The global aerosol-climate model ECHAM-HAM, version 2: sensitivity to improvements in process representations. *Atmospheric Chemistry and Physics*, 12(19), 8911–8949. <https://doi.org/10.5194/acp-12-8911-2012>